Bandwidth controlled quantum phase transition between an easy-plane quantum spin Hall state and an s-wave superconductor

Disha Hou,[1] Yuhai Liu,[2,3] Toshihiro Sato,[4] Wenan Guo,[1,2,*] Fakher F. Assaad,[4,5,†] and Zhenjiu Wang[6,‡]

[1] *Department of Physics, Beijing Normal University, Beijing 100875, China*
[2] *Beijing Computational Science Research Center, 10 East Xibeiwang Road, Beijing 100193, China*
[3] *School of Science, Beijing University of Posts and Telecommunications, Beijing 100876, China*
[4] *Institut für Theoretische Physik und Astrophysik, Universität Würzburg, 97074 Würzburg, Germany*
[5] *Würzburg-Dresden Cluster of Excellence ct.qmat, Am Hubland, 97074 Würzburg, Germany*
[6] *Max-Planck-Institut für Physik komplexer Systeme, Dresden 01187, Germany*

arXiv:2207.04803v3 [cond-mat.str-el] 30 Mar 2023

The quantum spin Hall state can be understood in terms of spontaneous O(3) symmetry breaking. Topological skyrmion configurations of the O(3) order parameter vector carry a charge 2e, and as shown previously, when they condense, a superconducting state is generated. We show that this topological route to superconductivity survives easy-plane anisotropy. Upon reducing the O(3) symmetry to O(2)$\times$ Z_2, skyrmions give way to merons that carry a unit charge. On the basis of large-scale auxiliary field quantum Monte Carlo simulations, we show that at the particle-hole symmetric point, we can trigger a continuous and direct transition between the quantum spin Hall state and s-wave superconductor by condensing pairs of merons. This statement is valid in both strong and weak anisotropy limits. Our results can be interpreted in terms of an easy-plane deconfined quantum critical point. However, in contrast to the previous studies in quantum spin models, our realization of this quantum critical point conserves $U(1)$ charge, such that skyrmions are conserved.

I. INTRODUCTION

Topology is a key factor for understanding phase transitions. In the Kosterlitz-Thouless theory,[1] an O(2) local order parameter in two-dimensional space allows for the definition of the vortex, the proliferation of which drives the transition. Let us stay in two-dimensional space, $\boldsymbol{x} = (x, y)$, but consider an O(3) local order parameter $\boldsymbol{n}(\boldsymbol{x})$ with the unit norm. This combination of space and order parameter defines a winding number,[2]

$$\frac{1}{4\pi}\int d^2\boldsymbol{x}\, \boldsymbol{n}\cdot\partial_x\boldsymbol{n}\times\partial_y\boldsymbol{n}. \tag{1}$$

For smooth configurations, this quantity is quantized and counts the winding of the unit vector on the unit sphere: a skyrmion. We can now reduce the O(3) symmetry to $O(2)\times Z_2$. In the context of spin systems, this would correspond to restricting the O(3) symmetry to O(2) transformations around, say, the z-axis and a change of sign of the third component of the $\boldsymbol{n}$-vector. Assuming that energetics favor the $\boldsymbol{n}$-vector to be in-plane (i.e., vanishing z-component) then the topological excitations will correspond to vortices in the x-y plane. Due to the normalization condition, the $\boldsymbol{n}$-vector at the core of the vortex will have to point along the z-direction. Since the $\boldsymbol{n}$-vector lies in the x-y plane at infinity, the integrand of Eq. 1 vanishes at infinity and the integral takes half-integer values: a meron.

The above considerations acquire different interpretations depending upon the specifics of the local order parameter. In this paper, it corresponds to the *order-parameter* of the quantum-spin Hall state. In particular, let $\hat{H}_0 = -v_F\sum_{\boldsymbol{p},\sigma,i=1,2}\hat{\boldsymbol{\Psi}}^\dagger_\sigma(\boldsymbol{p})ip_i\gamma_0\gamma_i\hat{\boldsymbol{\Psi}}_\sigma(\boldsymbol{p})$ be the Hamiltonian akin to graphene in the absence of interactions,[3] using the notation of Ref. 4. Inclusion of the quantum spin Hall mass term leads to:

$$\hat{H} = \hat{H}_0 + \int_V d\boldsymbol{x}\boldsymbol{N}(\boldsymbol{x})\cdot\hat{\boldsymbol{\Psi}}^\dagger_\sigma(\boldsymbol{x})i\gamma_0\gamma_3\gamma_5\boldsymbol{\sigma}_{\sigma,\sigma'}\hat{\boldsymbol{\Psi}}_{\sigma'}(\boldsymbol{x}). \tag{2}$$

The order parameter $\boldsymbol{N}$ can be normalized to unity $\boldsymbol{n} = \boldsymbol{N}/|\boldsymbol{N}|$ if, as will be the case in our model, the single-particle gap, that is proportional to the length of $\boldsymbol{N}$, does not vanish. Furthermore, $\boldsymbol{n}$ is odd under charge conjugation such that the expression in Eq. (1) carries the same quantum numbers as the charge density ρ measured with respect to half-filling. In particular, in Ref. 5 it is shown that

$$\rho(\boldsymbol{x}) = \frac{2e}{4\pi}\boldsymbol{n}\cdot\partial_x\boldsymbol{n}\times\partial_y\boldsymbol{n} \tag{3}$$

such that the skyrmion (meron pairs) carry charge 2e. Since topological defects of one phase carry the charge of the other, their proliferation will lead to a symmetry-broken state. In the above discussion, we have considered the quantum spin Hall (QSH) state where the skyrmions (or pairs of merons) carry charge 2e and their proliferation leads to a superconducting state. Alternatively, one could consider the three spin-density wave mass terms. In this case, the skyrmion creation/annihilation process would acquire a phase under the spatial rotation of the lattice. This proliferation of skyrmions is the essence of so-called 'deconfined' quantum critical points (DQCPs).[6–8]

* waguo@bnu.edu.cn
† assaad@physik.uni-wuerzburg.de
‡ zhwang@pks.mpg.de

The above discussion takes place in the continuum, and some type of regularization is needed to carry out numerical simulations. Starting with magnetic phases, where the topological defects carry a U(1) rotational charge, a lattice regularization leads to additional symmetry breaking terms that may lead to subtleties since they do not exist in the expected IR field theory.[9,10] For instance for a square lattice regularization scheme, U(1) rotational symmetry gives way to a $\mathbb{Z}_4$ invariance of the valence bond solid (VBS) state. This regularization-induced symmetry reduction introduces novel operators that have to be argued to be irrelevant at the critical point. In particular, in the framework of the CP^1 field theory of spinon coupled to a U(1) gauge field,[6] this symmetry reduction allows for the creation of quadruple monopoles of the gauge field.

Although the Z_4 lattice symmetry-breaking field is relevant in the VBS state, a necessary condition for the continuous nature of the transition into an xy-antiferromagnetic (AFM) phase is that this symmetry-breaking field is irrelevant at the critical point. Numerically, AFM-VBS phase transitions in the easy-plane case have clear first-order signatures in most cases.[11–17] Among numerical works, Desai et. al.,[17] in p emphasize the absence of the continuous transition in any easy-plane spin system: the authors generally claimed the absence of the easy-plane deconfined fixed point without considering the effect of quadruple monopoles. However, could it be that the Z_4 symmetry-breaking field introduces a runaway flow, leading to a first-order transition?

Instead of encoding the U(1) symmetry as a rotational invariance, one can encode it in terms of charge conservation. Importantly, charge conservation will not be broken by lattice regularization. Following the work of Ref. 18 and 19 we set up a set of designer Hamiltonians which have the potential to realize an easy-plane DQCP without quadruple monopoles. A dynamically generated QSH insulating state which spontaneously breaks the O(2) spin rotational symmetry emerges from a Dirac semi-metal via a spin-orbital interaction. Our particular interest lines in the phase transition between the QSH and s-wave superconducting (SSC) states.

The fermion basis introduces a simple but much more provoking picture: meron defects of the QSH order parameter which carry a unit of electron charge are the fundamental excitation at the critical point; on the other side of the transition, the condensation of meron-pair creation/annihilation operators forms the superconducting state. Importantly, the U(1) charge conservation broken by the SSC phase is an exact symmetry of our lattice Hamiltonian, meaning that quadruple monopoles are absent by definition.

The aim of this work is to systematically search for the existence of an easy-plane DQCP without monopoles. The continuity of phase transitions does not only depend on symmetry.[20,21] In our lattice model, a model parameter that is related to the *strength* of the easy-plane anisotropy continuously tunes the energy gap of meron configurations of a QSH order parameter. Regardless of the strength of the anisotropy and in contrast to lattice spin models, our model shows no obvious signs of first-order transitions. We argue that this transition flows to the easy-plane DQCP.

The paper is organized as follows. In Sec. II we introduce our lattice Hamiltonian, the quantum Monte Carlo algorithm, as well as basic observables. The numerical results are shown in Sec. III, beginning with the ground state phase diagram and followed by a detailed investigation of the nature of the phase transitions. Finally, we draw conclusions and give an outlook in Sec. IV.

II. MODEL AND METHODS

We consider a model of Dirac fermions in $2+1$ dimensions on the honeycomb lattice with Hamiltonian

$$\hat{H}_t = -t \sum_{\langle \boldsymbol{i},\boldsymbol{j}\rangle} (\hat{\boldsymbol{c}}_{\boldsymbol{i}}^\dagger \hat{\boldsymbol{c}}_{\boldsymbol{j}} + H.c.). \tag{4}$$

Here, the spinor $\hat{\boldsymbol{c}}_{\boldsymbol{i}}^\dagger = \left(\hat{c}_{\boldsymbol{i},\uparrow}^\dagger, \hat{c}_{\boldsymbol{i},\downarrow}^\dagger\right)$ where $\hat{c}_{\boldsymbol{i},\sigma}^\dagger$ creates an electron in a Wannier state centered around lattice site $\boldsymbol{i}$ with z-component of spin σ. This term accounts for nearest-neighbor hopping. The interaction term that we consider reads:

$$\begin{aligned}\hat{H}_\lambda = -\lambda \sum_{\hexagon} \Bigg[&\left(\sum_{\langle\langle \boldsymbol{ij}\rangle\rangle \in \hexagon} \hat{J}^x_{\boldsymbol{i},\boldsymbol{j}} \right)^2 + \left(\sum_{\langle\langle \boldsymbol{ij}\rangle\rangle \in \hexagon} \hat{J}^y_{\boldsymbol{i},\boldsymbol{j}} \right)^2 \\ &+\Delta \left(\sum_{\langle\langle \boldsymbol{ij}\rangle\rangle \in \hexagon} \hat{J}^z_{\boldsymbol{i},\boldsymbol{j}} \right)^2 \Bigg]\end{aligned} \tag{5}$$

where $\hat{\boldsymbol{J}}_{\boldsymbol{i},\boldsymbol{j}} \equiv i\nu_{\boldsymbol{ij}} \hat{\boldsymbol{c}}_{\boldsymbol{i}}^\dagger \boldsymbol{\sigma} \hat{\boldsymbol{c}}_{\boldsymbol{j}} + H.c.$ The components of $\boldsymbol{\sigma} = (\sigma^x, \sigma^y, \sigma^z)$ are the Pauli spin-1/2 matrices. This term is a plaquette interaction involving next-nearest-neighbor pairs $\langle\langle \boldsymbol{ij}\rangle\rangle$ of sites and phase factors $\nu_{\boldsymbol{ij}} = \pm 1$ identical to the Kane-Mele model,[22] see also Ref. 18.

The Hamiltonian $\hat{H} = \hat{H}_t + \hat{H}_\lambda$ with $\Delta = 1$ has been studied in Ref. 18. A dynamically generated QSH insulator that breaks $SU(2)$ spin rotational symmetry spontaneously is found at intermediate interacting strength (λ), separating a Dirac semi-metal(DSM) state at small λ and an SSC state at large λ. The DSM-QSH transition belongs to the Gross-Neveu Heisenberg universality class[23] whereas the QSH-SSC transition falls into the class of DQCP. In the current work, we focus on the case of $\Delta \in [0, 1)$ where the $SU(2)$ spin rotational symmetry is reduced to $U(1) \times Z_2$.

We used the ALF (Algorithms for Lattice Fermions) implementation[24] of the well-established auxiliary-field quantum Monte Carlo (QMC) method.[25–27] Because $\lambda > 0$ and $\Delta > 0$, we can use a real Hubbard-Stratonovich decomposition for the perfect square term. We set the

TABLE I. Projection length θ at different values of Δ and L.

lattice size	anisotropy strength		
	$\Delta = 0.1$	$\Delta = 0.5$	$\Delta = 0.75$
$L = 6$	15	15	15
$L = 9$	21	21	21
$L = 12$	24	24	24
$L = 15$	42	36	36
$L = 18$	42	36	36

imaginary time interval $\Delta\tau = 0.2$ and choose a symmetric Trotter decomposition to ensure the hermiticity of the imaginary time propagation in the Monte Carlo simulations.[18] Additionally, a checkerboard decomposition is applied to the exponential of hopping matrix $\hat{H}_t$. For each field configuration, time-reversal symmetry and charge are conserved. Hence the eigenvalues of the fermion determinant occur in complex conjugate pairs, and we do not suffer from the negative sign problem.[28] We simulated lattices with $L \times L$ unit cells (each containing two Dirac fermions) and periodic boundary conditions. Following our previous work,[19] we used a projective version of the algorithm (PQMC).[27,29,30] This algorithm is based on the form:

$$\langle \hat{O} \rangle = \lim_{\theta\to\infty} \frac{\left\langle \Psi_T | e^{-\theta\hat{H}} \hat{O} e^{-\theta\hat{H}} | \Psi_T \right\rangle}{\left\langle \Psi_T | e^{-2\theta\hat{H}} | \Psi_T \right\rangle}. \tag{6}$$

Provided that the trial wave function $|\Psi_T\rangle$ is not orthogonal to the ground state, $\langle \hat{O} \rangle$ corresponds to the ground state expectation value of the observable $\hat{O}$. To avoid the negative sign problem, we consider the same time-reversal symmetric trial wave function as the one used in Ref. 19. We explicitly checked the projection convergence to the ground state at each system size and each Δ: simulations are performed at $L = 6, 9, 12, 15, 18$ and the values of projection length θ for ground state calculation are listed in Tab. I.

The basic measurements in our QMC simulations are equal time correlation functions in real space:

$$S^O(\boldsymbol{r}) \equiv \frac{1}{L^2} \sum_n \sum_{\boldsymbol{r}'} \langle \hat{O}^\dagger_{\boldsymbol{r},n} \hat{O}_{\boldsymbol{r}+\boldsymbol{r}',n} \rangle, \tag{7}$$

and the structure factor:

$$S^O_{m,n}(\boldsymbol{q}) \equiv \frac{1}{L^2} \sum_{\boldsymbol{r},\boldsymbol{r}'} e^{\mathrm{i}\boldsymbol{q}\cdot(\boldsymbol{r}-\boldsymbol{r}')} \langle \hat{O}^\dagger_{\boldsymbol{r},m} \hat{O}_{\boldsymbol{r}',n} \rangle, \tag{8}$$

where $\hat{O}_{\boldsymbol{r},n}$ is a local operator with $\boldsymbol{r}$ denoting the unit cell and n denoting the intra unit-cell dependence that we will refer to as orbital.

For instance, the spin-orbit coupling operators correspond to $\hat{\boldsymbol{O}}_{\boldsymbol{r},n} = \hat{\boldsymbol{J}}_{\boldsymbol{r}+\boldsymbol{\delta}_n,\boldsymbol{r}+\boldsymbol{\eta}_n}$. Here n runs over the six next-nearest neighbor bonds of the corresponding hexagon with legs $\boldsymbol{r}+\boldsymbol{\delta}_n$ and $\boldsymbol{r}+\boldsymbol{\eta}_n$ $(n = 1, 2, ...6)$, see Fig. 1. To detect QSH ordering which breaks the $O(2)$ spin rotational symmetry, we calculate the structure factor matrix associated with the X and Y components of $\hat{\boldsymbol{O}}_{\boldsymbol{r},n}$

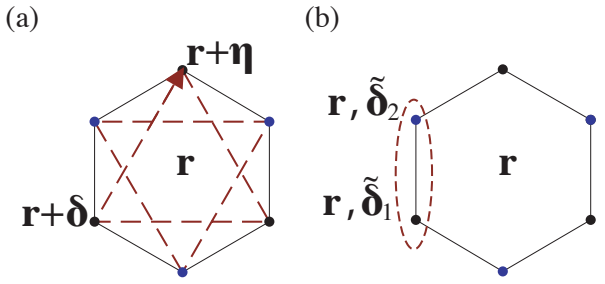


FIG. 1. Honeycomb plaquette illustrating (a) the spin-orbit coupling operator $\hat{\boldsymbol{J}}_{\boldsymbol{r}+\boldsymbol{\delta}_n,\boldsymbol{r}+\boldsymbol{\eta}_n}$ and (b) the pairing operator $\hat{\eta}^+_{\boldsymbol{r},\tilde{\boldsymbol{\delta}}_{\boldsymbol{a}}}$.

$$S^{\mathrm{QSH}}_{m,n}(\boldsymbol{q}) \equiv \frac{1}{L^2} \sum_{\boldsymbol{r},\boldsymbol{r}'} e^{\mathrm{i}\boldsymbol{q}\cdot(\boldsymbol{r}-\boldsymbol{r}')} \langle \hat{O}^X_{\boldsymbol{r},m} \hat{O}^X_{\boldsymbol{r}',n} + \hat{O}^Y_{\boldsymbol{r},m} \hat{O}^Y_{\boldsymbol{r}',n} \rangle, \tag{9}$$

with $m, n = 1, 2, ...6$. We also consider the structure factor matrix associated with the Z component of $\hat{\boldsymbol{O}}_{\boldsymbol{r},n}$

$$S^{\mathrm{QSH}_Z}_{m,n}(\boldsymbol{q}) \equiv \frac{1}{L^2} \sum_{\boldsymbol{r},\boldsymbol{r}'} e^{\mathrm{i}\boldsymbol{q}\cdot(\boldsymbol{r}-\boldsymbol{r}')} \langle \hat{O}^Z_{\boldsymbol{r},m} \hat{O}^Z_{\boldsymbol{r}',n} \rangle. \tag{10}$$

The physical meaning of this quantity will be discussed in Sec. III.

To detect SSC ordering which breaks $U(1)$ charge conservation, we consider the following structure factor matrix:

$$S^{\mathrm{SSC}}_{a,b}(\boldsymbol{q}) \equiv \frac{1}{L^2} \sum_{\boldsymbol{r},\boldsymbol{r}'} e^{\mathrm{i}\boldsymbol{q}\cdot(\boldsymbol{r}-\boldsymbol{r}')} [\langle \hat{\eta}^+_{\boldsymbol{r},\tilde{\boldsymbol{\delta}}_a} \hat{\eta}^-_{\boldsymbol{r}',\tilde{\boldsymbol{\delta}}_b} \rangle + \langle \hat{\eta}^-_{\boldsymbol{r},\tilde{\boldsymbol{\delta}}_a} \hat{\eta}^+_{\boldsymbol{r}',\tilde{\boldsymbol{\delta}}_b} \rangle], \tag{11}$$

with $a, b = 1, 2$, denoting the A(B) sublattice, where the s-wave pairing operator is defined as

$$\hat{\eta}^+_{\boldsymbol{r},\tilde{\boldsymbol{\delta}}_{\boldsymbol{a}}} = \hat{c}^\dagger_{\boldsymbol{r}+\tilde{\boldsymbol{\delta}}_{\boldsymbol{a}},\uparrow} \hat{c}^\dagger_{\boldsymbol{r}+\tilde{\boldsymbol{\delta}}_{\boldsymbol{a}},\downarrow}. \tag{12}$$

Here $\tilde{\delta}_a$ runs over the two orbitals in unit cell $\boldsymbol{r}$, see Fig. 1.

We use Eq. 9 and Eq.11 to calculate the order parameter:

$$m^O = \sqrt{\frac{\Lambda_1(S^O(\boldsymbol{Q}))}{L^2}} \tag{13}$$

Here, $\Lambda_1()$ indicates the largest eigenvalue of the corresponding matrix in orbital space, O denotes QSH and SSC order parameters, and $\boldsymbol{Q} = (0, 0)$. The corresponding eigenvector will determine the orbital structure. This

is of particular importance for the QSH state since we expect it to reflect the sign structure ν_{ij} of the Kane-Mele model.

To locate the critical points and study the critical properties, after diagonalizing the corresponding structure factors, we calculated the renormalization-group invariant correlation ratio

$$R^O \equiv 1 - \frac{S^O(\boldsymbol{Q}+\Delta\boldsymbol{q})}{S^O(\boldsymbol{Q})} \tag{14}$$

using the largest eigenvalue S^O (O = QSH, QSH$_z$, SSC); $\boldsymbol{Q} = (0,0)$ is the ordering wave vector and $\boldsymbol{Q}+\Delta\boldsymbol{q}$ is a neighboring wave vector with $|\Delta\boldsymbol{q}| = \frac{4\pi}{\sqrt{3}L}$. By definition, $R^O \to 1$ for $L \to \infty$ in the corresponding ordered state, whereas $R^O \to 0$ in the disordered state. At the critical point, R^O is scale-invariant for sufficiently large L so that the results for different system sizes cross.

III. QUANTUM MONTE CARLO RESULTS

In this section we will first provide the ground state phase diagram and then will proceed to investigate the nature of the phase transitions.

A. Ground state phase diagram

As mentioned previously, we are interested in the parameter range of $\Delta \in [0,1)$ where the spin rotational symmetry of the Hamiltonian $\hat{H} = \hat{H}_t + \hat{H}_\lambda$ is lowered to $U(1)\times Z_2$. The DSM and SSC states found in the $SU(2)$ symmetric case[18] ($\Delta = 1$) are naturally stable against weak easy-plane anisotropy $\Delta \approx 1$ since both states are spin rotational invariant. Furthermore, since time reversal symmetry is not broken by our symmetry reduction, we expect the QSH phase to be equally stable. To confirm the above, we can use the mean-field approach introduced in Ref. 19 that carries over to the anisotropic case. Due to the Dirac nature of the kinetic term in Eq. 4, we foresee the robustness of the DSM phase in the weakly interacting case. On the other hand, the *attractive* nature of $\hat{H}_\lambda$ term (for $\Delta \geq 0$, $\lambda > 0$) suggests that the mean-field picture in the large λ case[19] will still favor an SSC instability. Finally, the dynamically generated QSH state at intermediate values of λ will be restricted to the $U(1)$ plane in the current case. We present the mean-field phase diagram in Fig. 2. The details of the calculations are summarized in Appendix A. It is worth mentioning that, in the mean-field analysis, the QSH and SSC orderings coexist in a large λ region of the phase diagram, see Fig. 2. This is a natural consequence of the anti-commuting nature of the two Dirac masses. In this case, the fermion band gap is given by the norm of the four-component order parameter accounting for the QSH ($m_{\rm QSH}$) and SSC ($m_{\rm SSC}$) orders:

$$\Delta_{\rm MF} \propto \sqrt{m^2_{\rm QSH} + m^2_{\rm SSC}}. \tag{15}$$

Hence, developing superconducting ordering in the background of a QSH state can simply minimize the mean-field free energy[19] in the *large* λ limit.

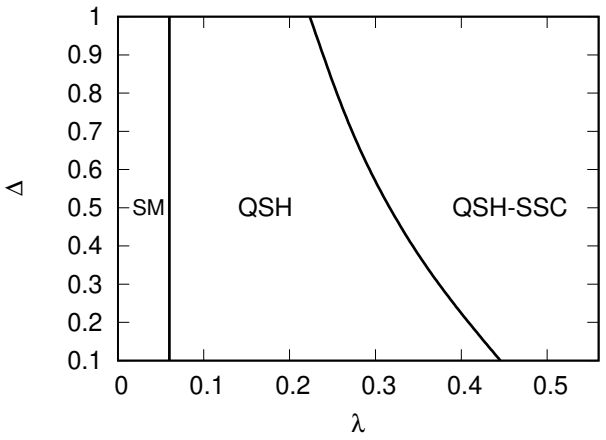


FIG. 2. Mean-field phase diagram at zero temperature as a function of Δ and λ.

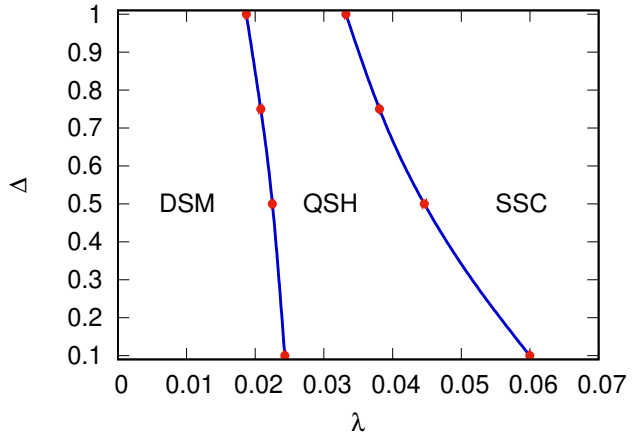


FIG. 3. Ground state phase diagram in the (Δ,λ) plane which covers the range of $\Delta \in [0.1,1]$. The DSM-QSH and QSH-SSC phase boundaries at $\Delta = 0.1, 0.5$, and 0.75 are estimated from PQMC simulations in this paper. The phase boundaries of $SU(2)$ symmetric Hamiltonian (the overline of $\Delta = 1$) are from Ref.[18]

We summarize the exact ground state phase diagram in (Δ,λ) plane based on QMC results in Fig. 3, where the overline $\Delta = 1$ corresponds to the $SU(2)$ symmetric model that was studied in Ref.18. Generally speaking, we found a DSM state at weak interaction (small λ region), an SSC state at strong interaction (large λ region), as well as a $U(1)$ broken QSH state at an intermediate region.

The numerical simulations that we performed cover three horizontal lines as a function of λ: $\Delta = 0.1$, 0.5 and 0.75. As shown in Fig. 4(b), Fig. 5(b), and Fig. 6(b), the QSH correlation ratio R^{QSH} increases toward 1 at intermediate values of λ, indicating a robust QSH state for all

three cases. We have checked explicitly that the eigenvector corresponding to the largest eigenvalue matches the sign structure ν_{ij} of the Kane-Mele model. Furthermore, in Appendix D we have used the flux-insertion scheme presented in Ref. 31 to probe for the topological invariant. The DSM-QSH and QSH-SSC phase boundaries are estimated by fitting the equal-time correlation ratios of the two largest lattice sizes $L = 15$ and $L = 18$ according to the following function

$$f(L, \lambda) = R_c + a_1(\lambda - \lambda_c)L^{1/\nu} + a_2(\lambda - \lambda_c)^2 L^{2/\nu}. \quad (16)$$

The details of the fit are listed in Tab. II and Tab. III. Remarkably, the critical values of λ where superconducting order develops, as shown by the crossing points of R^{SSC} in Fig. 4(a), Fig. 5(a), and Fig. 6(a), match the values of λ where the QSH order vanishes. This indicates that, regardless of the strength of anisotropy, direct phase transitions exist between the QSH and SSC phases. The order parameters give consistent results, as shown in Fig. 7.

The comparison of the mean-field, Fig. 2, and QMC, Fig. 3, phase diagrams are very instructive. The transition from the DSM to QSH insulator at $\Delta < 1$ belongs to the U(1) Gross Neveu universality class. The essence of this transition, a symmetry-breaking induced electronic mass generation, is captured at the mean-field level. In fact, an ϵ-expansion around the upper critical dimension accounts rather well for this transition for the SO(3)[32,33] and U(1) cases.[34] It is hence not unexpected that the comparison between the mean-field, Fig. 2, and QMC, Fig. 3, phase diagrams is *good* for this transition. In contrast, the competition and interplay between the QSH and SSC phases are radically different at the mean-field and QMC levels. We interpret this mismatch as a hint that topology – not accounted for at the mean-field level – is crucial for the understanding of the intertwinement of the QSH and SSC phases. Of particular importance is that the QMC phase diagram does not show a coexistence of the QSH and SSC phases. The nature of the transition will be discussed in the next section.

TABLE II. DSM-QSH crossing points λ_c.

anisotropy	λ_c	χ_r^2	O
$\Delta = 0.1$	0.0243(2)	0.14	QSH
$\Delta = 0.5$	0.0225(2)	2.7	QSH
$\Delta = 0.75$	0.0208(3)	0.81	QSH

Our QSH insulator at zero temperature is also a gapless phase, reflecting the emergence of Goldstone modes upon breaking the global XY symmetry. Therefore, both the spin current operators $\hat{J}^{x,y}$ and the corresponding angular momentum operator $\hat{S}^z$ reveal gapless excitations around zero momentum. On the other hand, merons in this phase are another low-energy excitation with a finite gap. Roughly speaking, the binding energy of pairs of merons, is higher in the case of strong anisotropy. The numerical evidence that merons bind can be deduced from the spectral functions presented in Appendix C. A comparison between the single particle and superconducting spectral functions shows that the cost of adding a pair is less than twice the single-particle gap. This binding energy can be tuned to zero by increasing the interaction, thus triggering a direct transition to a superconducting state.

TABLE III. QSH-SSC crossing points λ_c.

anisotropy	λ_c	χ_r^2	O
$\Delta = 0.1$	0.06006(8)	0.08	QSH
	0.05988(2)	2.41	SSC
$\Delta = 0.5$	0.0448(2)	19.87	QSH
	0.04444(4)	3.77	SSC
$\Delta = 0.75$	0.03829(4)	1.67	QSH
	0.03788(3)	3.44	SSC

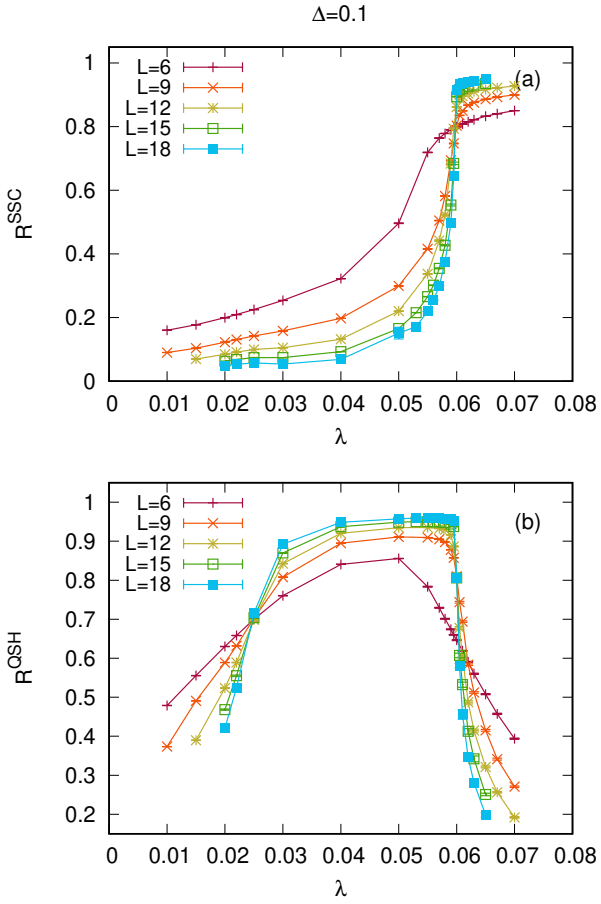


FIG. 4. Equal-time correlation ratio $R^{\rm SSC}$ (a) and $R^{\rm QSH}$ (b) as a function of λ for $\Delta = 0.1$.

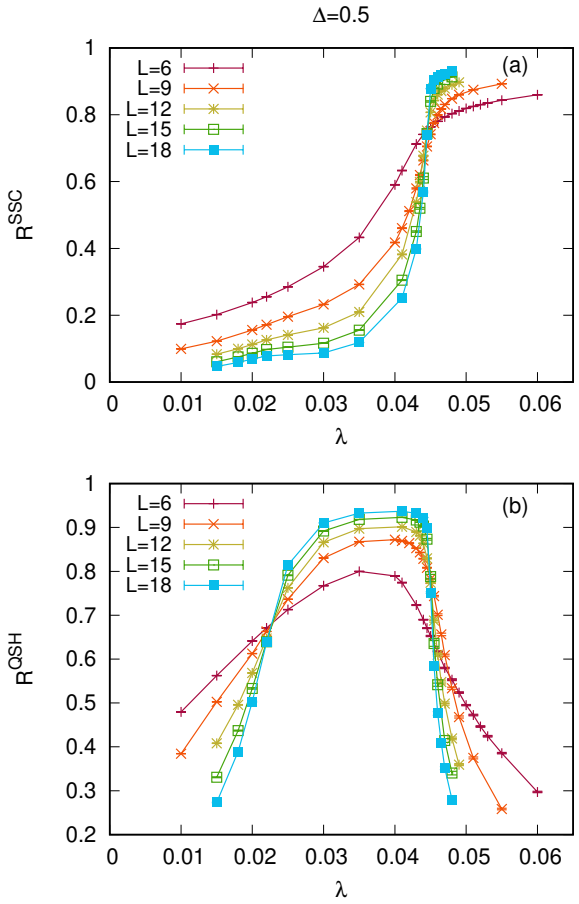


FIG. 5. Same as Fig. 4 for $\Delta = 0.5$.

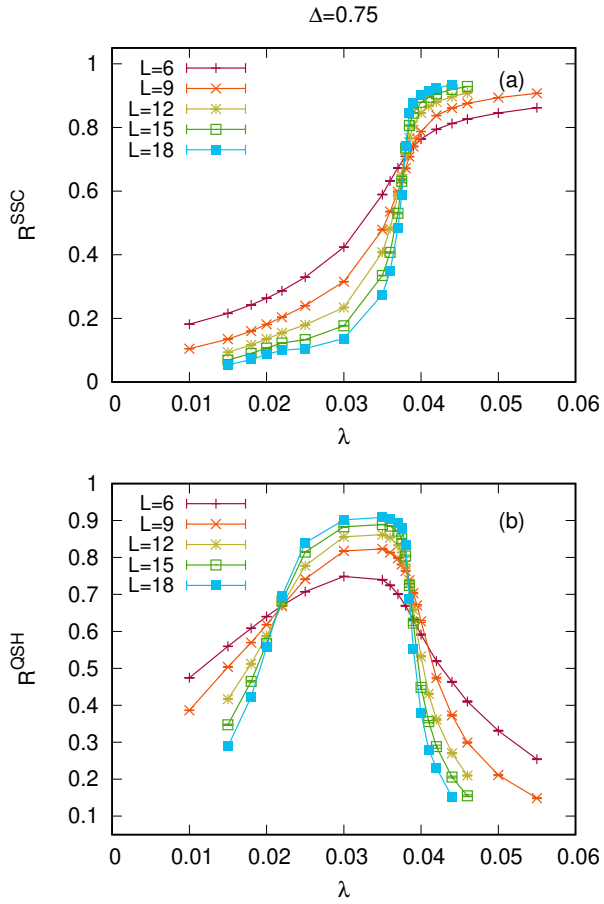


FIG. 6. Same as Fig. 4 for $\Delta = 0.75$.

B. Nature of the QSH-SSC phase transition

Our most important result is the seemingly continuous nature of the QSH-SSC transition.

The QSH-SSC transition has only bosonic excitations at low energy. To characterize this, we extrapolate the fermionic single particle gap Δ_{sp} from Green's function:

$$\sum_{\sigma}\langle c_{\boldsymbol{k},\sigma}(\tau)c^{\dagger}_{\boldsymbol{k},\sigma}(0)\rangle \propto e^{-\Delta_{\rm sp}\tau}, \tag{17}$$

at $\boldsymbol{k} = M \equiv (0, \frac{2\pi}{\sqrt{3}})$. Figure. 8 demonstrates that Δ_{sp} remains nonzero across the QSH-SSC transition at λ_c for all three considered values of the anisotropy.

In the following step, we inquire whether the QSH-SSC transition is continuous or not. Considering that the computational cost of the AFQMC scales as θL^3 with θ being the projection length, we do not apply the commonly used method for detecting first-order transitions, such as analyzing the finite-size behavior of the histogram of order parameters or the behavior of the Binder cumulant. Instead, we study the correlation length to reflect the nature of the phase transitions. A continuous phase transition is characterized by a diverging correlation length in the thermodynamic limit: $\xi \propto |\lambda - \lambda_c|^{-\nu}$. On the other hand, for a first-order transition, the correlation length saturates to a finite value. We use the real-space, equal-time correlation functions $S^O(\boldsymbol{r})$ of the order parameter to define the correlation length[35]

$$\xi^O \equiv \sqrt{\frac{\sum_{\boldsymbol{r}} |\boldsymbol{r}|^2 S^O(\boldsymbol{r})}{\sum_{\boldsymbol{r}} S^O(\boldsymbol{r})}} \tag{18}$$

where $S^O(\boldsymbol{r})$ is defined in Eq. 7. For continuous symmetry breaking, an issue with this definition is that it picks up the correlation lengths along both the longitudinal and the transverse directions. Hence without a specific symmetry-breaking pinning field to resolve the longitudinal direction, the correlation length ξ in Eq. (18) is well defined only in the disordered state or at the critical point. Therefore, we discard the data for the QSH (SSC) correlation length in the QSH (SSC) state.

As depicted in Fig. 9(a), Fig. 10(a) and Fig. 11(a), around transition points at different values of Δ, the correlation length ξ of both the QSH and SSC order parameters grow with system size L, without any tendency of saturation. We define the scaled correlation length ξ/L as the ratio between the correlation length and system size. As shown in Fig. 9(b), Fig. 10(b), and Fig. 11(b),

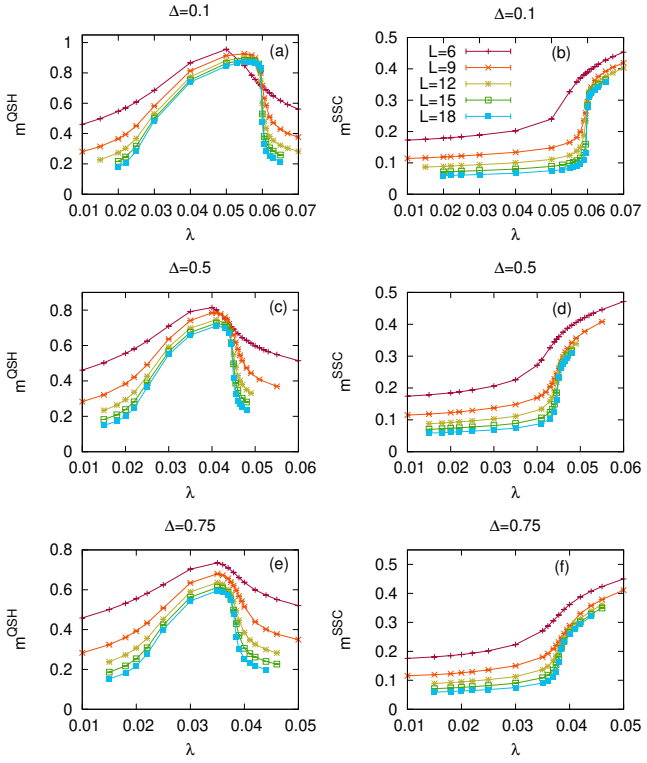


FIG. 7. QSH and SSC order parameter as a function of λ, for $\Delta = 0.1$ ((a) and (b)), 0.5 ((c) and (d)) and 0.75 ((e) and (f)).

for both the QSH and SSC correlation lengths, the ratios for different system sizes cross at the same point, suggesting that the correlation length diverges with L. The divergence of correlation lengths indicates the continuous nature of the phase transition.

It is worth mentioning that we observe an amazing match of the value of the scaled correlation length ξ/L for different anisotropy strengths Δ. The fact that the same value of ξ/L at the three transition points implies that all three QSH-SSC phase transition points correspond to the same fixed point. ξ/L is a dimensionless quantity which is a renormalization-group invariant at the critical point. This number is claimed to be universal in a $(2+1)$ dimensional system with conformal invariance. On a lattice system, this universal number is not only pinned by the scaling dimension of the order parameter but also by the microscopic couplings in different directions, the boundary conditions, and the shape of the system (e.g. the aspect ratio).[36,37] In our case, the only difference between the three different values of Δ is the intrinsic spin anisotropy which is not related to the lattice geometry, such that ξ/L should be universal if all three transitions at $\Delta = 0.1, 0.5$ and 0.75 belong to the same universality class. We also observe the interesting behavior that QSH and SSC operators cross at the same value of ξ/L at the transition point. This also indicates the identical value of the anomalous dimension η between

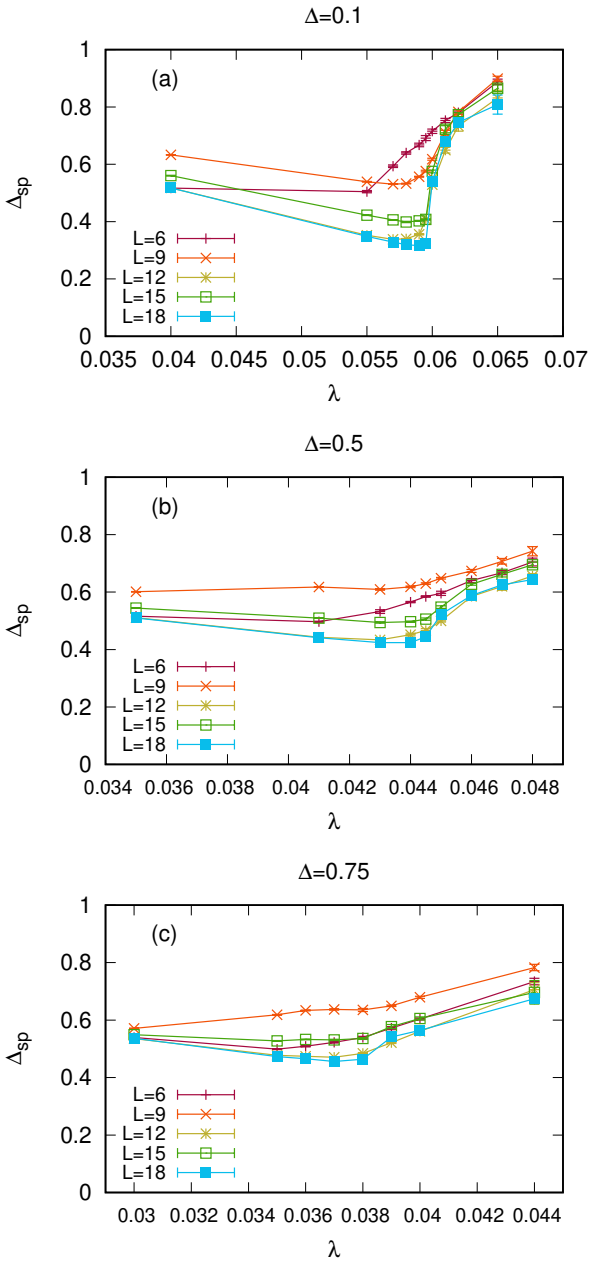


FIG. 8. Single particle gap Δ_{sp} across the QSH-SSC transition for $\Delta = 0.1$ (a), $\Delta = 0.5$ (b), and $\Delta = 0.75$ (c), respectively.

the two order parameters, which is significant evidence of an emergent O(4) symmetry.[8,38]

We also calculate the first-order partial derivative of the free energy density with respect to the coupling strength λ,

$$\frac{\partial f}{\partial \lambda} = \frac{1}{L^2}\frac{1}{\lambda}\langle \hat{H}_\lambda \rangle, \tag{19}$$

to study the nature of the phase transition. This approach requires no information of the order parameter (and the associated symmetry breaking). In the case of a

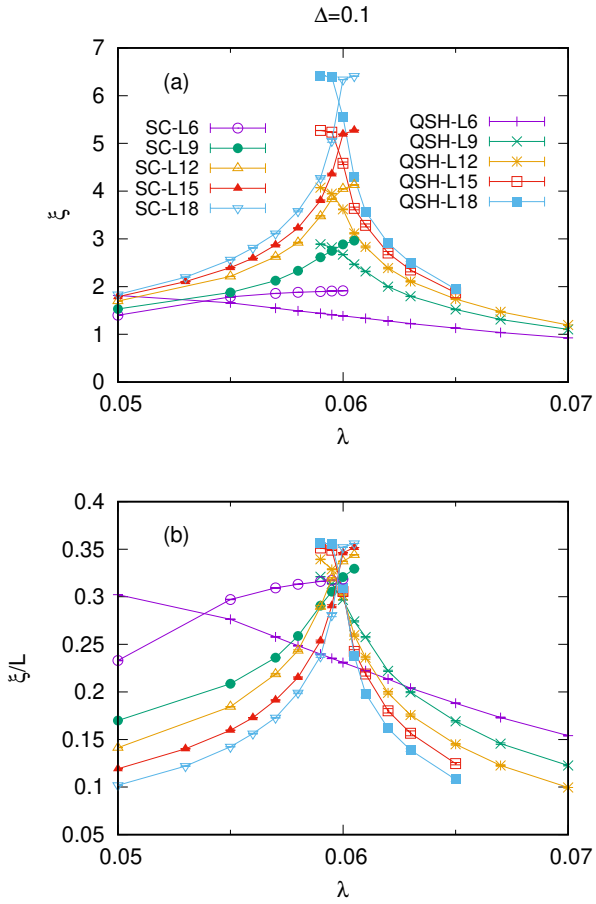


FIG. 9. Correlation length (a) and scaled correlation length (b) in disordered phase for $\Delta = 0.1$.

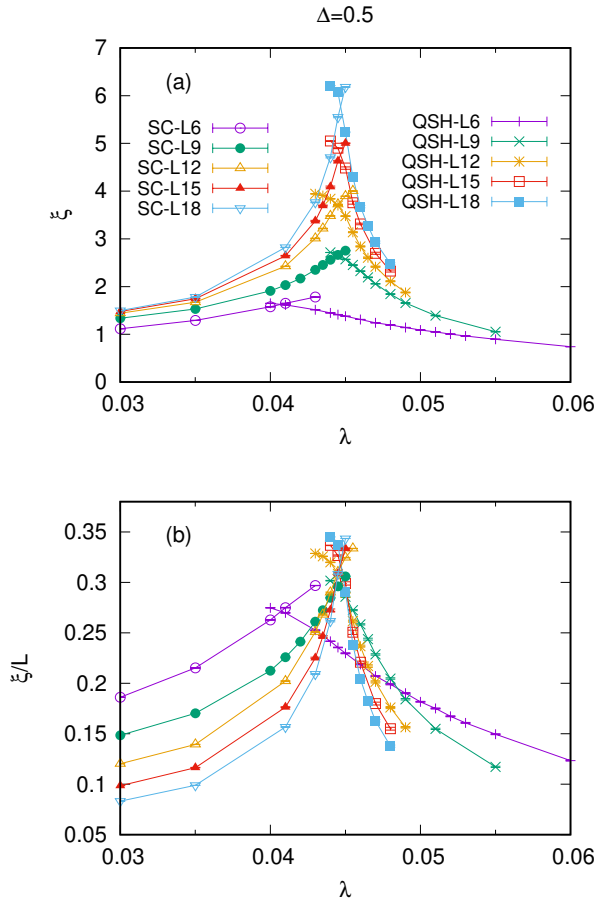


FIG. 10. Same as Fig. 9 for $\Delta = 0.5$.

first order transition, when the system size is much larger than correlation length ξ, one expects a discontinuity in this derivative at the transition point. Figure 12 shows $\partial f/\partial\lambda$ as a function of λ in the vicinity of the QSH-SSC transition point for $\Delta = 0.1$, 0.5 and 0.75. Our data reveal no clear signs of a jump for the accessible system sizes in this study. This is consistent with the aforementioned correlation length analyses.

In the strong anisotropic case $\Delta = 0.1$, the slope of the curve scales up moving towards the transition point when increasing the system size. This result may be interpreted as the signature of a 'weakly first-order' transition. Around a continuous transition point, the derivative of the free energy scales as

$$\frac{\partial f}{\partial \lambda} \propto |\lambda - \lambda_c|^{(d+z)\nu - 1} \tag{20}$$

in the thermodynamic limit. For a 'weakly first-order' transition, one expects a 'pseudo critical' phenomenon where the $\nu(L)$ estimated from finite sizes would approach $1/(d+z)$ as L reaches ξ,[39] such that $\partial f/\partial\lambda$ asymptotically shows a jump. However, we won't be able to conclude the nature of transition at $\Delta = 0.1$ since it is not clear whether the finite-size slope diverges or saturates upon approaching the thermodynamic limit. On the other hand, the robustness of the slope in the case of $\Delta = 0.5$ and $\Delta = 0.75$ as shown in Fig. 12(b) and (c), indicates clear continuous phase transitions, unless there exists a non-diverging ξ that is significantly larger than L.

We now consider the Z-component of the QSH correlations, Eq. 10. In the DSM and at the DSM to QSH transition the single particle gap vanishes such that this quantity is expected to decay as a power-law. In particular, in the DSM the scaling dimension of the fermion operator is given by $\frac{d}{2}$ ($d = 2$ is the dimensionality) such that the Z-QSH as well as XY-QSH correlation functions are expected to decay as r^{-4} with r being the distance. At the DSM to QSH transition the scaling dimensions of both quantities will differ. For equal time correlations, and in $d = 2$, power-law decay leads to a divergence in the structure factor provided that the scaling dimension of the operator is smaller that unity. In the DSM the scaling dimension of the QSH operators is two, and we do not pick up any a signal: as apparent from Fig. 13, the correlation ratio decays as a function of system size. However at the DSM-QSH transition it is worth noting a distinct cusp in the S^{QSH_z} correlation ratio especially at $\Delta = 0.75$ (see Fig. 13(c)). In the ordered XY-QSH

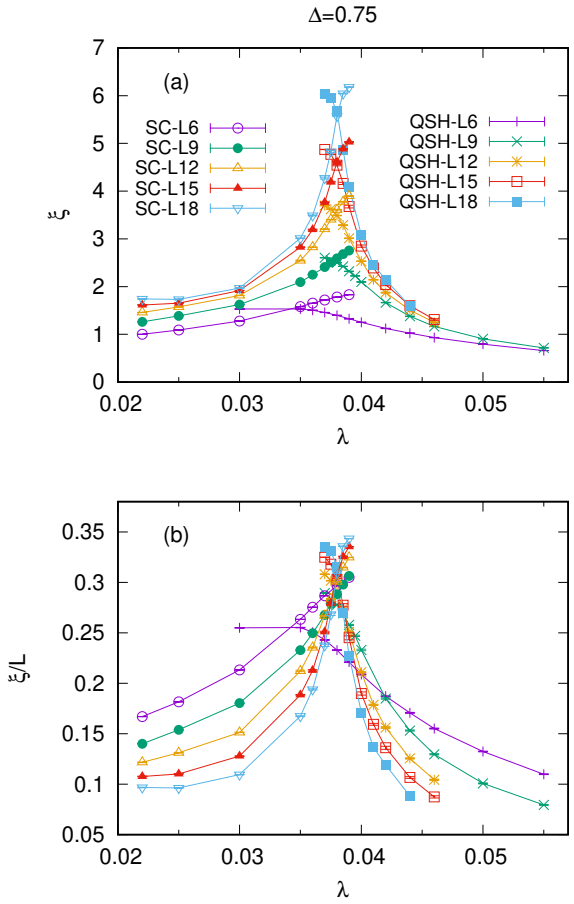


FIG. 11. Same as Fig. 9 for $\Delta = 0.75$.

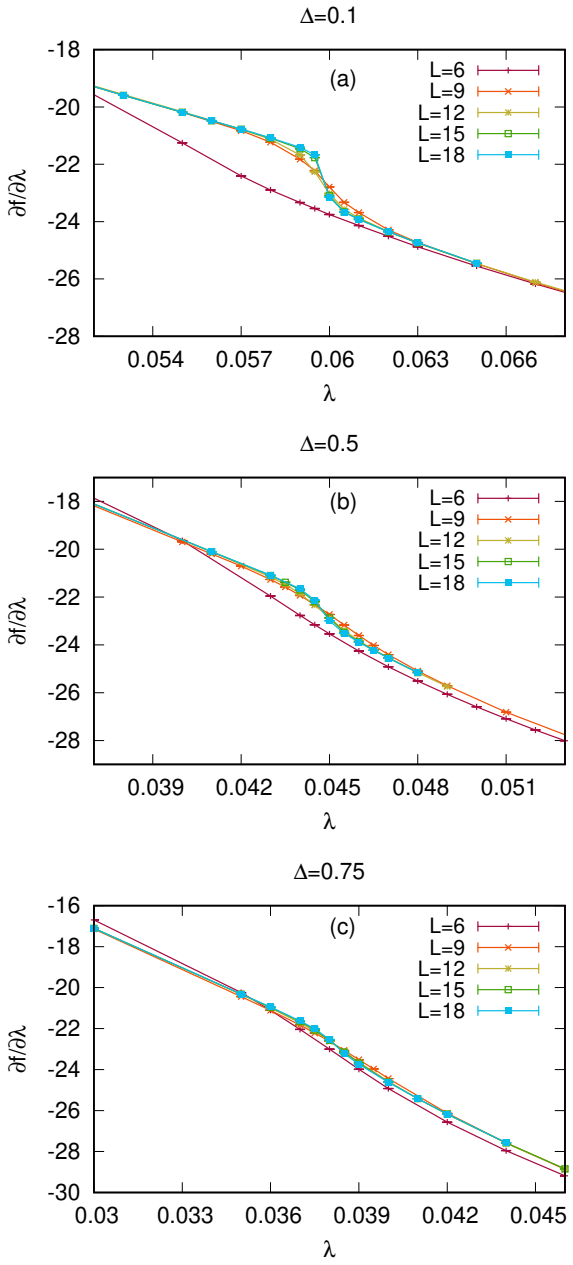


FIG. 12. Free-energy derivative $\partial f/\partial\lambda$ as a function of λ in the vicinity of the QSH-SSC transition point, for $\Delta = 0.1$ (a), $\Delta = 0.5$ (b), and $\Delta = 0.75$ (c), respectively.

phase, the anisotropy opens a gap in the Z-QSH spectrum, leading to a reduction in the Z-QSH correlation ratio as a function of system size (see Fig. 13). In the SSC phase the spin degrees of freedom are gapped, such that the Z-QSH correlations decay exponentially. Again, in this phase, the Z-QSH correlation ratio decays as a function of system size (see Fig. 13).

It hence comes as a surprise that at the QSH-SSC transition, we see a distinct cusp in the Z-QSH correlation ratio. This suggests that at this transition

$$S^{\mathrm{QSH}}(\boldsymbol{Q}) \propto L^{1-\eta_{XY}} \tag{21}$$

and

$$S^{\mathrm{QSH}_Z}(\boldsymbol{Q}) \propto L^{1-\eta_Z} \tag{22}$$

albeit with different scaling dimensions. Here, $\boldsymbol{Q} \equiv (0,0)$. Assuming the same criticality as in Ref. 40, $\eta_{XY} \approx 0.13$ and $\eta_Z \approx 0.91$. Given the large anomalous dimension, η_Z, it is more advantageous to consider the *susceptibility* as defined in Eq. B11 of Appendix B. For Lorentz invariant systems, this quantity scales as $L^{2-\eta_Z}$ and suffers less from background effects. Fig. 19 plots the correlation ratio as obtained from the *susceptibility*. While we can observe clear cusps at the QSH-SSC transition we cannot unambiguously claim that this quantity scales to a finite value in the thermodynamic limit.

In Fig. 14 we show the spin-orbit, $\hat{J}^{XY}$, and the pairing, $\hat{\eta}^{+}(\hat{\eta}^{-})$, dynamical correlation functions at the QSH-SSC critical point at $\Delta = 0.75$. For the definition of the spectral functions as well as for further data, we refer the reader to Appendix C. The spectral functions display gapless excitations with the very same velocity. This stands in accord with emergent Lorentz invariance. The $\hat{J}^{Z}$ spectral function, Fig. 14 (c), allows for an interpre-

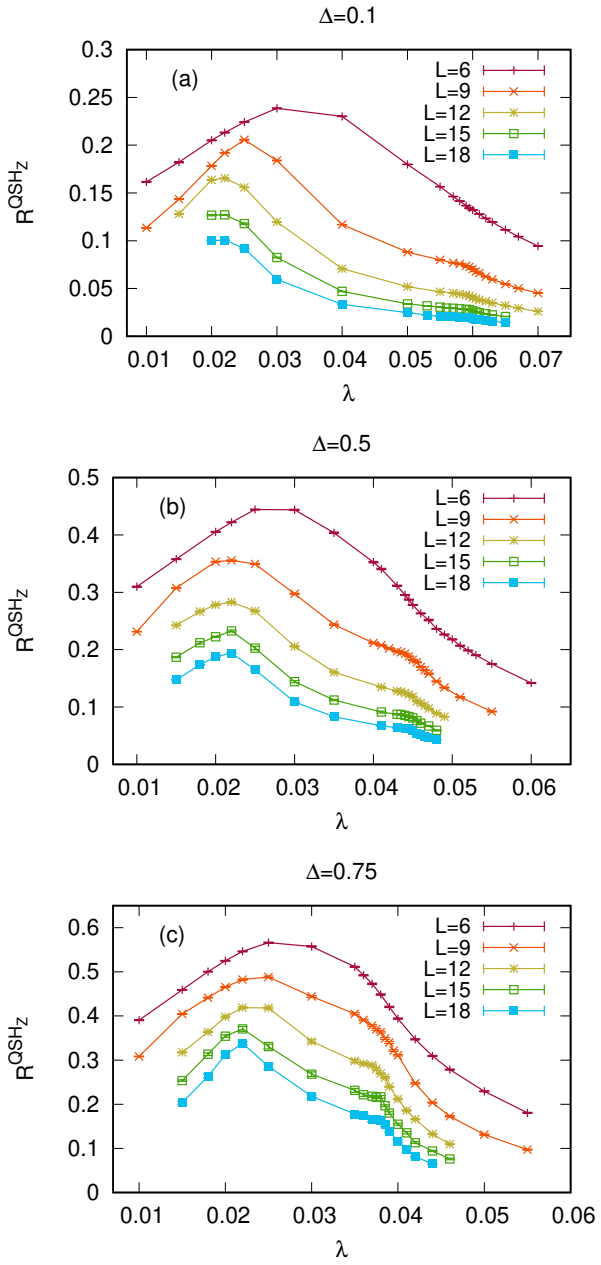


FIG. 13. Equal-time correlation ratio R^{QSHz} for $\Delta = 0.1$ (a), $\Delta = 0.5$ (b), and $\Delta = 0.75$ (c), respectively.

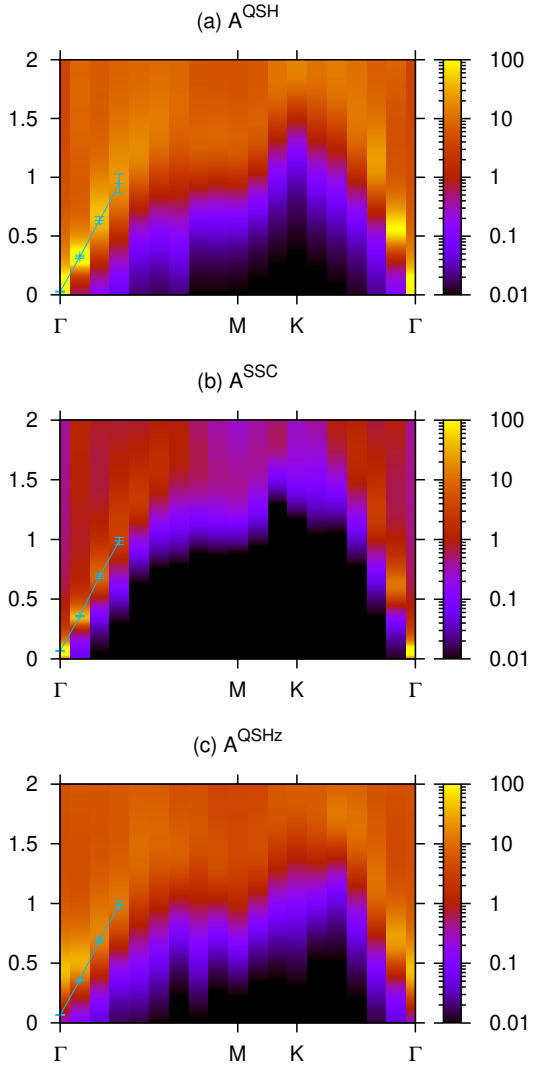


FIG. 14. QSH (a), SSC (b), and QSHz (c) dynamical spectrum at the QSH-SSC critical point ($\lambda = 0.038$) for $\Delta = 0.75$. Here, $L = 18$. Blue lines in (a) and (b) are the momentum dependence of the extrapolated excitation gap of $\hat{J}^{XY}$ and $\hat{\eta}^{+}(\hat{\eta}^{-})$ operators. The blue line in (c) is copied from the SSC dispersion relation in (b) to guide the eye.

tation in terms of gapless excitations at the Γ point albeit with small spectral weight at low energies.

IV. DISCUSSIONS AND OUTLOOK

Our model realizes an easy-plane quantum spin Hall insulating state that emerges from spontaneous U(1) broken spin symmetry, with a unnormalized three component order parameter $\boldsymbol{N}$ defined in space-time. The norm of the order parameter defines the single-particle gap. By tuning a single parameter λ at a given anisotropy strength, we observe DSM-QSH as well as QSH-SSC transitions. At the DSM-QSH transition, the amplitude of the order parameter vanishes and the single-particle gap closes. We understand this transition in terms of Gross-Neveu-XY universality, the exponents of which should be equivalent to those computed in Ref. 34.

The focus of the paper, is on the QSH-SSC transition. Here, the QMC results show that i) the single particle gap does not close at the transition and ii) in contrast to mean-field calculations, our results on lattice sizes up to $L = 18$ support a continuous and direct transition for all considered values of the anisotropy. We can safely omit the scenario of fine tuning, where acci-

dentally, the two transitions occur at the same value of λ. This statement is based on the numerical observation that we consistently see a direct transition for all values of the anisotropy. Furthermore, the energetics are affected by the value of the imaginary time step we use in our simulations. Were we at a fine tuning point, then we would have noticed substantial changes in our results when varying the imaginary time step.

Since the single particle gap remains finite we can normalize the order parameter vector $\boldsymbol{n} = \boldsymbol{N}/|\boldsymbol{N}|$, and attempt to understand the transition in terms of fluctuations of $\boldsymbol{n}$. In this context, and as discussed in the introduction, skyrmions or pairs of merons carry charge 2e and condense at the transition. This suggests that our QSH-SSC transitions flow to the easy-plane deconfined quantum critical point irrespective of the anisotropy parameter. This is also supported numerically by the observed *universal* value of the scaled correlation length upon changing the anisotropy. The scaled correlation length takes the same value for the QSH and SSC fluctuations at the easy-plane DQCP which supports an emergent O(4) symmetry at least on intermediate length scales. Our model summarizes the very first calculations of this critical point in a lattice Hamiltonian where the lattice regularization does not break the IR symmetries of the putative field theory. As a consequence, our lattice regularization does not introduce quadruple monopoles as in the easy-plane JQ model. We refer the reader to Appendix E for a detailed discussion of this point.

One of the characteristics of the easy-plane DQCP, is the emergence of deconfined spinons at the critical point. In particular, one can adopt a CP^1 representation of the order parameter

$$\boldsymbol{n} \equiv z^\dagger \boldsymbol{\sigma} z \qquad z^\dagger z = 1 \tag{23}$$

(see Appendix E). The claim of DQC[7] is that the CP^1 theory supports a deconfined phase at the critical point. The questions then becomes how we can provide numerical evidence for this. Fractionalized spinons are not directly measurable at the DQCP point since they do not directly correspond to any local second quantized operators. However, the existence of deconfined spinons suggests that at criticality the Z-component of the correlation functions of the QSH order parameter shows power-law decay since it just corresponds to spinon correlation functions. Our numerics support this point of view.

To place our results in a broader perspective, we can ask the question of whether designer Hamiltonians with higher symmetry can impact criticality. Although it is well known that phase transitions numerically observed in easy-plane lattice spin models have a higher tendency to be discontinuous in the anisotropic case, two possible underlying physical interpretations remain possible. First, the relevance of the Z_4 symmetry-breaking perturbation at the easy-plane deconfined fixed point generally leads to a runaway flow, explaining the first order nature of transition. Second, even if symmetry-breaking terms due to lattice regularization (e.g., $O(4)$ down to $U(1) \times U(1)$ or $U(1) \times Z_4$) are imposed to be zero, the easy-plane DQCP may not even exist in any unitary conformal field theory. In this context our results may be understood in terms of proximity to a DQCP that is not accessible to our simulation space. This could correspond to a DQCP in the complex plane[8] or in dimensions close to d=2.[41,42]

ACKNOWLEDGMENTS

The authors gratefully acknowledge the Gauss Centre for Supercomputing e.V. for funding this project by providing computing time on the GCS Supercomputer SUPERMUC-NG at Leibniz Supercomputing Centre. F.F.A. acknowledges the DFG for funding via Würzburg-Dresden Cluster of Excellence on Complexity and Topology in Quantum Matter ct.qmat (EXC 2147, Project ID 390858490) as well as the SFB1170 on Topological and Correlated Electronics at Surfaces and Interfaces. T.S. acknowledges funding from the Deutsche Forschungsgemeinschaft under Grant No. SA 3986/1-1. Y.L. was supported by the China Postdoctoral Science Foundation under Grants No. 2019M660432 and No. 2020T130046 as well as the National Natural Science Foundation of China under Grants No. 11947232 and No.U1930402. D.H. and W.G. were supported by the National Natural Science Foundation of China under Grants No. 12175015 and No. 11734002.

[1] J. M. Kosterlitz and D. J. Thouless, Journal of Physics C: Solid State Physics **6**, 1181 (1973).
[2] E. Fradkin, Field Theories of Condensed Matter Physics, 2nd ed. (Cambridge University Press, 2013).
[3] A. H. C. Neto, F. Guinea, N. M. R. Peres, K. S. Novoselov, and A. K. Geim, Rev. Mod. Phys. **81**, 109 (2009).
[4] I. F. Herbut, V. Juričić, and B. Roy, Phys. Rev. B **79**, 085116 (2009).
[5] T. Grover and T. Senthil, Phys. Rev. Lett. **100**, 156804 (2008).
[6] T. Senthil, L. Balents, S. Sachdev, A. Vishwanath, and M. P. A. Fisher, Phys. Rev. B **70**, 144407 (2004).
[7] T. Senthil, A. Vishwanath, L. Balents, S. Sachdev, and M. P. A. Fisher, Science **303**, 1490 (2004).
[8] C. Wang, A. Nahum, M. A. Metlitski, C. Xu, and T. Senthil, Phys. Rev. X **7**, 031051 (2017).
[9] A. W. Sandvik, Phys. Rev. Lett. **98**, 227202 (2007).

[10] H. Shao, W. Guo, and A. W. Sandvik, Science **352**, 213 (2016).
[11] A. Kuklov, N. Prokof'ev, B. Svistunov, and M. Troyer, Annals of Physics **321**, 1602 (2006), july 2006 Special Issue.
[12] J. D'Emidio and R. K. Kaul, Phys. Rev. B **93**, 054406 (2016).
[13] A. W. Sandvik, S. Daul, R. R. P. Singh, and D. J. Scalapino, Phys. Rev. Lett. **89**, 247201 (2002).
[14] S. Kragset, E. Smørgrav, J. Hove, F. S. Nogueira, and A. Sudbø, Phys. Rev. Lett. **97**, 247201 (2006).
[15] A. Sen, K. Damle, and T. Senthil, Phys. Rev. B **76**, 235107 (2007).
[16] J. D'Emidio and R. K. Kaul, Phys. Rev. Lett. **118**, 187202 (2017).
[17] N. Desai and R. K. Kaul, Phys. Rev. B **102**, 195135 (2020).
[18] Y. Liu, Z. Wang, T. Sato, M. Hohenadler, C. Wang, W. Guo, and F. F. Assaad, Nature Communications **10**, 2658 (2019).
[19] Z. Wang, Y. Liu, T. Sato, M. Hohenadler, C. Wang, W. Guo, and F. F. Assaad, Phys. Rev. Lett. **126**, 205701 (2021).
[20] E. Domany, M. Schick, and R. H. Swendsen, Phys. Rev. Lett. **52**, 1535 (1984).
[21] H. W. J. Blöte, W. Guo, and H. J. Hilhorst, Phys. Rev. Lett. **88**, 047203 (2002).
[22] C. L. Kane and E. J. Mele, Phys. Rev. Lett. **95**, 146802 (2005).
[23] D. J. Gross and A. Neveu, Phys. Rev. D **10**, 3235 (1974).
[24] F. F. Assaad, M. Bercx, F. Goth, A. Götz, J. S. Hofmann, E. Huffman, Z. Liu, F. P. Toldin, J. S. E. Portela, and J. Schwab, SciPost Phys. Codebases , 1 (2022).
[25] R. Blankenbecler, D. J. Scalapino, and R. L. Sugar, Phys. Rev. D **24**, 2278 (1981).
[26] S. White, D. Scalapino, R. Sugar, E. Loh, J. Gubernatis, and R. Scalettar, Phys. Rev. B **40**, 506 (1989).
[27] F. Assaad and H. Evertz, in Computational Many-Particle Physics, Lecture Notes in Physics, Vol. 739, edited by H. Fehske, R. Schneider, and A. Weiße (Springer, Berlin Heidelberg, 2008) pp. 277–356.
[28] C. Wu and S.-C. Zhang, Phys. Rev. B **71**, 155115 (2005).
[29] G. Sugiyama and S. Koonin, Annals of Physics **168**, 1 (1986).
[30] S. Sorella, S. Baroni, R. Car, and M. Parrinello, EPL (Europhysics Letters) **8**, 663 (1989).
[31] F. F. Assaad, M. Bercx, and M. Hohenadler, Phys. Rev. X **3**, 011015 (2013).
[32] F. F. Assaad and I. F. Herbut, Phys. Rev. X **3**, 031010 (2013).
[33] Y. Liu, Z. Wang, T. Sato, W. Guo, and F. F. Assaad, Phys. Rev. B **104**, 035107 (2021).
[34] Y. Otsuka, K. Seki, S. Sorella, and S. Yunoki, Phys. Rev. B **98**, 035126 (2018).
[35] F. Parisen Toldin, M. Hohenadler, F. F. Assaad, and I. F. Herbut, Phys. Rev. B **91**, 165108 (2015).
[36] G. Kamieniarz and H. W. J. Blote, Journal of Physics A: Mathematical and General **26**, 201 (1993).
[37] X. Qian, Y. Deng, Y. Liu, W. Guo, and H. W. J. Blöte, Phys. Rev. E **94**, 052103 (2016).
[38] T. Sato, M. Hohenadler, and F. F. Assaad, Phys. Rev. Lett. **119**, 197203 (2017).
[39] S. Iino, S. Morita, N. Kawashima, and A. W. Sandvik, Journal of the Physical Society of Japan **88**, 034006 (2019), https://doi.org/10.7566/JPSJ.88.034006.
[40] Y. Q. Qin, Y.-Y. He, Y.-Z. You, Z.-Y. Lu, A. Sen, A. W. Sandvik, C. Xu, and Z. Y. Meng, Phys. Rev. X **7**, 031052 (2017).
[41] A. Nahum, Phys. Rev. B **102**, 201116 (2020).
[42] R. Ma and C. Wang, Phys. Rev. B **102**, 020407 (2020).
[43] P. D. Francesco, P. Mathieu, and D. Senechal, Conformal Field Theory (Springer Verlag, Berlin, Heidelberg, New York, 1997) p. Good for Lie Algebras. At least very short and compact.
[44] K. S. D. Beach, (2004), cond-mat/0403055.
[45] X.-L. Qi and S.-C. Zhang, Phys. Rev. Lett. **101**, 086802 (2008).
[46] E. Fradkin, Field Theories of Condensed Matter Physics, 2nd ed. (Cambridge University Press, 2013).
[47] F. D. M. Haldane, Phys. Rev. Lett. **61**, 1029 (1988).

Appendix A: Mean field calculation

In this appendix, we present our mean-field calculation. Expanding Eq. 5 of the main text as

$$\begin{aligned} H_\lambda =& -\lambda \sum_{\hexagon} \left[\left(\sum_{\langle\langle ij\rangle\rangle \in \hexagon} \hat{J}^x_{i,j} \right)^2 + \left(\sum_{\langle\langle ij\rangle\rangle \in \hexagon} \hat{J}^y_{i,j} \right)^2 \right. \\ & \left. + \Delta \left(\sum_{\langle\langle ij\rangle\rangle \in \hexagon} \hat{J}^z_{i,j} \right)^2 \right] \\ =& -\lambda \sum_{\hexagon} \sum_{\langle\langle ij\rangle\rangle} \sum_{\langle\langle i'j'\rangle\rangle \neq \langle\langle ij\rangle\rangle} \hat{\boldsymbol{J}}^{\boldsymbol{x}}_{\langle\langle i,j\rangle\rangle} \cdot \hat{\boldsymbol{J}}^{\boldsymbol{x}}_{\langle\langle i',j'\rangle\rangle} \\ & + \hat{\boldsymbol{J}}^{\boldsymbol{y}}_{\langle\langle i,j\rangle\rangle} \cdot \hat{\boldsymbol{J}}^{\boldsymbol{y}}_{\langle\langle i',j'\rangle\rangle} + \Delta \hat{\boldsymbol{J}}^{\boldsymbol{z}}_{\langle\langle i,j\rangle\rangle} \cdot \hat{\boldsymbol{J}}^{\boldsymbol{z}}_{\langle\langle i',j'\rangle\rangle} \\ & - \lambda \sum_{\hexagon} \sum_{\langle\langle ij\rangle\rangle} [+(4+2\Delta)\hat{\eta}^\dagger_i \hat{\eta}_j + h.c + ...] \end{aligned} \tag{A1}$$

where

$$\begin{aligned} \hat{\boldsymbol{J}}^{\alpha}_{\langle\langle i,j\rangle\rangle} &\equiv i\nu_{ij} \hat{c}^\dagger_i \boldsymbol{\sigma}^\alpha \hat{c}_j + H.c., \\ \hat{\eta}_i &\equiv \hat{c}_{i\downarrow} \hat{c}_{i\uparrow}, \quad \hat{\eta}^\dagger_i \equiv \hat{c}^\dagger_{i\uparrow} \hat{c}^\dagger_{i\downarrow}. \end{aligned} \tag{A2}$$

The ellipsis denotes terms that do not contribute to the SSC or QSH ordering within the mean-field decomposition.

The mean-field calculation involves selecting a polarization direction for the two components of the QSH and SSC order parameters. The calculation is done by numerically minimizing the free energy in the space of the two order parameters.

The two order parameters as a function of λ for the half-filled case are shown in Fig. 15. For all three different values of anisotropy, we observe a Dirac semimetal ($\phi_{QSH} = \phi_{SSC} = 0$), a pure QSH state ($\phi_{QSH} \neq 0, \phi_{SSC} = 0$) as well as coexistence of QSH and SSC phases ($\phi_{QSH} \neq 0, \phi_{SSC} \neq 0$).

The mean-field phase diagram in Fig. 2 shows greater stability of the QSH phase at stronger anisotropy. The reason for this becomes transparent when taking a glimpse at Eq. A1. Here Δ modulates the magnitude of the pair-hopping ($\hat{\eta}^\dagger_i \hat{\eta}_j + h.c.$) but not of the in-plane spin-orbit interactions ($\hat{J}^x_{\langle\langle i,j\rangle\rangle} \cdot \hat{J}^x_{\langle\langle i',j'\rangle\rangle} + x \leftrightarrow y$).

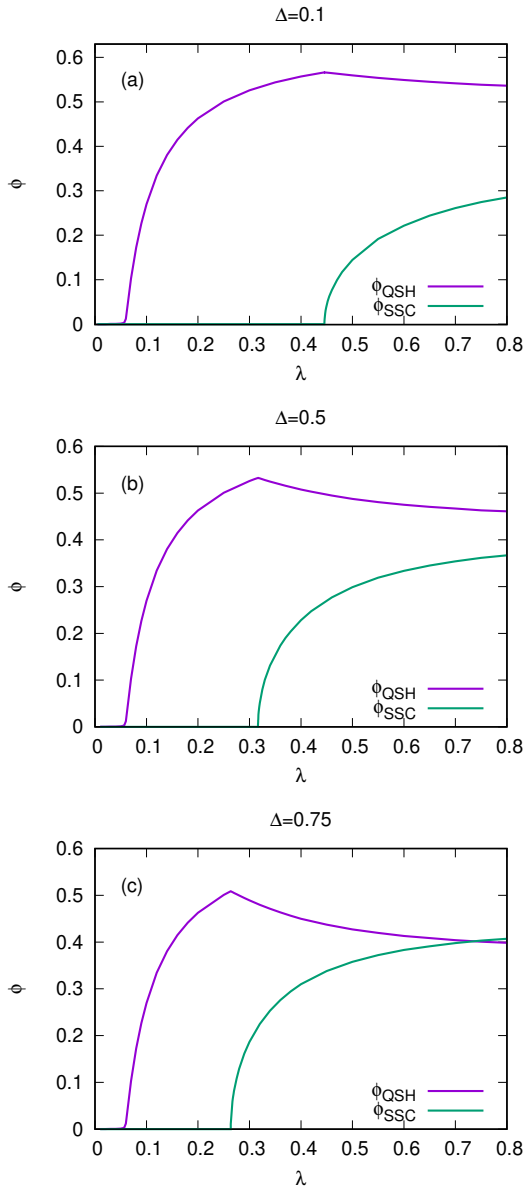


FIG. 15. Mean-field solution for the QSH and SSC order parameters as a function of λ for $\Delta = 0.1$ (a), $\Delta = 0.5$ (b), and $\Delta = 0.75$ (c), respectively.

Appendix B: Time displaced observables

To define susceptibilities in the realm of the zero temperature projective QMC algorithm used in this paper, we distinguish between observables $\hat{O}_{\boldsymbol{q}} = \frac{1}{\sqrt{N}} \sum_{\boldsymbol{r}} e^{i\boldsymbol{q}\cdot\boldsymbol{r}} \hat{O}_{\boldsymbol{r}}$ that commute or not with the Hamiltonian. Here, $N = L^2$. The key point is that for $\left[\hat{O}_{\boldsymbol{q}}, \hat{H}\right] = 0$,

$$\lim_{L\to\infty} \lim_{\beta\to\infty} \chi^{FT}(\boldsymbol{q},\beta,L) \neq \lim_{\beta\to\infty} \lim_{L\to\infty} \chi^{FT}(\boldsymbol{q},\beta,L) \quad \text{(B1)}$$

where

$$\chi^{FT}(\boldsymbol{q},\beta,L) = \int_0^\beta d\tau \left(\langle \hat{O}_{\boldsymbol{q}}(\tau)\hat{O}_{-\boldsymbol{q}}\rangle_T - \langle \hat{O}_{\boldsymbol{q}}\rangle_T \langle \hat{O}_{-\boldsymbol{q}}\rangle_T \right). \quad \text{(B2)}$$

In the above, $\langle \bullet \rangle_T = \frac{1}{Z}\mathrm{Tr}\left(e^{-\beta\hat{H}}\bullet\right)$ and $\hat{O}_{\boldsymbol{q}}(\tau) = e^{\tau\hat{H}}\hat{O}e^{-\tau\hat{H}}$. In particular, if the ground state is not degenerate then for $\left[\hat{O}_{\boldsymbol{q}}, \hat{H}\right] = 0$, $\lim_{L\to\infty}\lim_{\beta\to\infty}\chi^{FT}(\boldsymbol{q},\beta,L) = 0$, while $\lim_{\beta\to\infty}\lim_{L\to\infty}\chi^{FT}(\boldsymbol{q},\beta,L)$ does not necessarily vanish. An example is the spin susceptibility for a tight-binding model when the boundary conditions are chosen to ensure that the ground state is non-degenerate.

Let us now consider the case of finite momentum $\boldsymbol{q} \neq 0$ for a momentum-conserving Hamiltonian. Hence, $\left[\hat{O}_{\boldsymbol{q}}, \hat{H}\right] \neq 0$. Provided that the ground state is unique, we will show that the limits can be interchanged. Our starting point is the Lehmann representation:

$$\chi^{FT}(\boldsymbol{q},\beta,L) = \frac{\beta}{Z}\sum_n e^{-\beta E_n} \left|\langle n|\hat{O}_{\boldsymbol{q}}|n\rangle\right|^2 + \frac{1}{Z}\sum_{n\neq m} \frac{e^{-\beta E_m} - e^{-\beta E_n}}{E_m - E_n} \left|\langle n|\hat{O}_{\boldsymbol{q}}|m\rangle\right|^2 \quad \text{(B3)}$$

with $\hat{H}|n\rangle = E_n|n\rangle$ and $n \in \mathbb{N}$. Since we have assumed that $\boldsymbol{q} \neq 0$, the first term of the right-hand side of the above equation vanishes. Defining the density of state as, $N(E) = \lim_{L\to\infty}\sum_n \delta(E_n - E)$ we obtain:

$$\lim_{L\to\infty}\lim_{\beta\to\infty}\chi^{FT}(\boldsymbol{q},\beta,L) = \int dE N(E) \mathcal{P}\frac{1}{E-E_0} \times \left(\left|\langle E|\hat{O}_{\boldsymbol{q}}|E_0\rangle\right|^2 + \left|\langle E_0|\hat{O}_{\boldsymbol{q}}|E\rangle\right|^2 \right) \quad \text{(B4)}$$

and

$$\lim_{\beta\to\infty}\lim_{L\to\infty}\chi^{FT}(\boldsymbol{q},\beta,L) = N(E_0)\lim_{L\to\infty}\lim_{\beta\to\infty}\chi^{FT}(\boldsymbol{q},\beta,L) \quad \text{(B5)}$$

For a unique ground state, $N(E_0) = 1$. Hence, under the aforementioned assumptions we can interchange the limits and it makes sense to define susceptibilities within the ground state algorithm, where we first take the limit of zero temperature and then consider larger and larger lattices.

For practical purposes, we compute:

$$\chi(\boldsymbol{q}) = \int_0^\beta \mathrm{d}\tau \langle \hat{O}_{\boldsymbol{q}}(\tau)\hat{O}_{-\boldsymbol{q}}(0)\rangle - \langle \hat{O}_{\boldsymbol{q}}(\tau)\rangle\langle \hat{O}_{-\boldsymbol{q}}(0)\rangle \quad \text{(B6)}$$

where

$$\langle \hat{O}_{\boldsymbol{q}}(\tau)\hat{O}_{-\boldsymbol{q}}(0)\rangle \equiv \frac{\langle\Psi_T|e^{-\theta\hat{H}}e^{-(\beta-\tau)\hat{H}}\hat{O}_{\boldsymbol{q}}e^{-\tau\hat{H}}\hat{O}_{-\boldsymbol{q}}e^{-\theta\hat{H}}|\Psi_T\rangle}{\langle\Psi_T|e^{-(2\theta+\beta)\hat{H}}|\Psi_T\rangle} \quad \text{(B7)}$$

and $|\Psi_T\rangle$ is the trial wave function. We consider $\beta = L$ for all three values of Δ. As shown in the main text, we implicitly checked that for the considered size L, θ is chosen to be large enough to converge to the ground state.

Since the zero temperature approach to susceptibilities matches the result obtained with the *traditional* calculations, the scaling behaviors are identical. In particular in the vicinity of a Lorentz invariant (z=1) critical point we expect:

$$\chi(\boldsymbol{q}) \propto \xi^{-2\Delta+d+1} \quad \text{(B8)}$$

where the relationship between the scaling and anomalous dimensions reads $2\Delta = d + z - 2 + \eta$ and ξ is the diverging length scale in space and time. Replacing the length scale with the linear size of our system yields the desired result:

$$\chi(\boldsymbol{q}) \propto L^{2-\eta}. \quad \text{(B9)}$$

Hence, as for the finite temperature case, we expect at the critical point that χ suppresses background contributions of the non-singular part of free energy by an additional power (of the dynamical exponent). [18,43] Assuming Lorentz invariance at the easy-plane DQCP, this additional power is unity.

We define the susceptibilities of the QSH, SSC, and QSHz in B10, B11 and B12.

$$\chi^{\mathrm{QSH}}_{m,n}(\boldsymbol{q}) \equiv \frac{1}{L^2}\sum_{\boldsymbol{r},\boldsymbol{r'}}\int_0^\beta \mathrm{d}\tau e^{\mathrm{i}\boldsymbol{q}\cdot(\boldsymbol{r}-\boldsymbol{r'})} \langle \hat{O}^X_{\boldsymbol{r},m}(\tau)\hat{O}^X_{\boldsymbol{r'},n}(0) + \hat{O}^Y_{\boldsymbol{r},m}(\tau)\hat{O}^Y_{\boldsymbol{r'},n}(0)\rangle. \quad \text{(B10)}$$

$$\chi^{\mathrm{QSH}_z}_{m,n}(\boldsymbol{q}) \equiv \frac{1}{L^2}\sum_{\boldsymbol{r},\boldsymbol{r'}}\int_0^\beta \mathrm{d}\tau e^{\mathrm{i}\boldsymbol{q}\cdot(\boldsymbol{r}-\boldsymbol{r'})} \langle \hat{O}^Z_{\boldsymbol{r},m}(\tau)\hat{O}^Z_{\boldsymbol{r'},n}(0)\rangle. \quad \text{(B11)}$$

$$\chi^{\mathrm{SSC}}_{a,b}(\boldsymbol{q}) \equiv \frac{1}{L^2}\sum_{\boldsymbol{r},\boldsymbol{r'}}\int_0^\beta \mathrm{d}\tau e^{\mathrm{i}\boldsymbol{q}\cdot(\boldsymbol{r}-\boldsymbol{r'})} [\langle \hat{\eta}^+_{\boldsymbol{r},\widetilde{\boldsymbol{\delta}}_a}(\tau)\hat{\eta}^-_{\boldsymbol{r'},\widetilde{\boldsymbol{\delta}}_b}(0)\rangle + \langle \hat{\eta}^-_{\boldsymbol{r},\widetilde{\boldsymbol{\delta}}_a}(\tau)\hat{\eta}^+_{\boldsymbol{r'},\widetilde{\boldsymbol{\delta}}_b}(0)\rangle], \quad \text{(B12)}$$

After diagonalizing the corresponding three susceptibilities, we calculated the renormalization-group invariant correlation ratio:

$$R^O_\chi \equiv 1 - \frac{\chi^O(\boldsymbol{Q}+\Delta\boldsymbol{q})}{\chi^O(\boldsymbol{Q})} \quad \text{(B13)}$$

with using the largest eigenvalue $\chi^O(\boldsymbol{q})$ with O referring to SSC, QSH, and QSH$_z$, respectively. The ordering wave vector is $\boldsymbol{Q} = (0,0)$, and $|\Delta \boldsymbol{q}| = \frac{4\pi}{\sqrt{3}L}$. We note that since the superconducting order parameter breaks U(1) global charge symmetry and the QSH order parameter breaks inversion symmetry so that the conditions for inter-changing the limits of zero temperature and infinite size are satisfied.

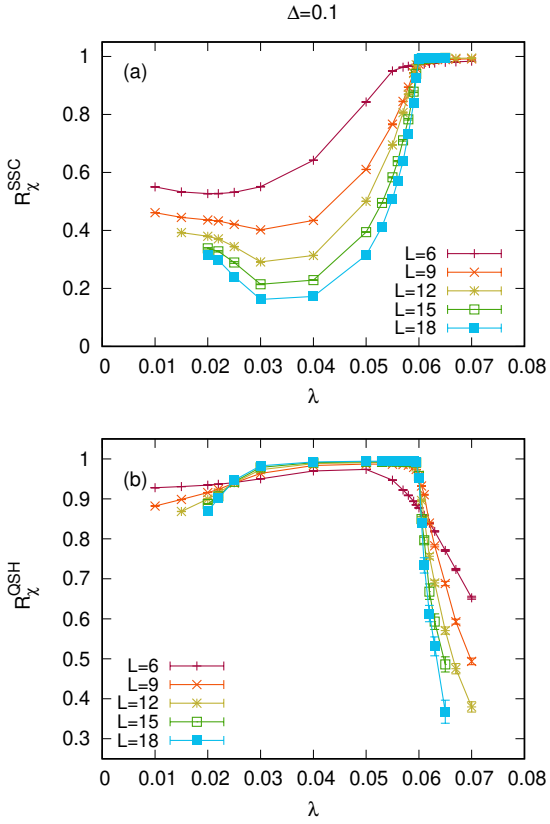


FIG. 16. Time displaced correlation ratio R_χ^{SSC} (a) and R_χ^{QSH} (b) as a function of λ for $\Delta = 0.1$.

The finite size behavior of R_χ^{QSH} and R_χ^{SSC} show no significant differences compared to the corresponding equal time correlations considered in the main text. As shown in Figs. 16, 17 and 18, the crossing points are consistent with the estimation of critical points from the main text. On the other hand, the scaling of $R_\chi^{\mathrm{QSH}_z}$ remains ambiguous: at the QSH-SSC transition point, this quantity decays toward zero for strong anisotropy ($\Delta = 0.1$). In the case of $\Delta = 0.5$ and 0.75 it could converge to a finite constant in thermodynamic limit; upon increasing the system sizes, its decreasing tendency is similar to the one from equal time correlation ratio in the main text.

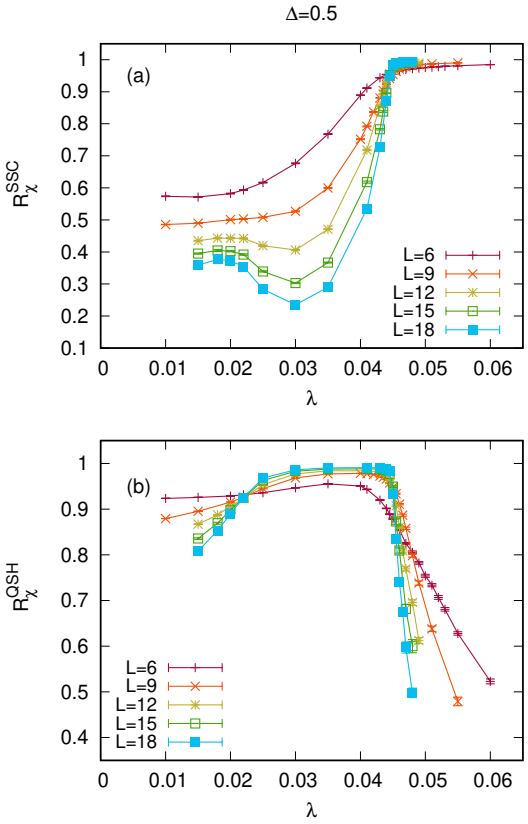


FIG. 17. Same as Fig. 16 for $\Delta = 0.5$.

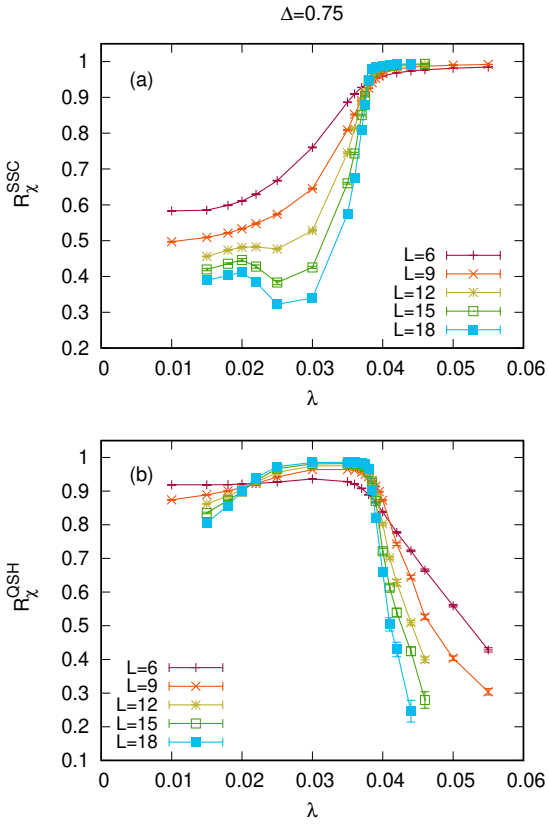


FIG. 18. Same as Fig. 16 for $\Delta = 0.75$.

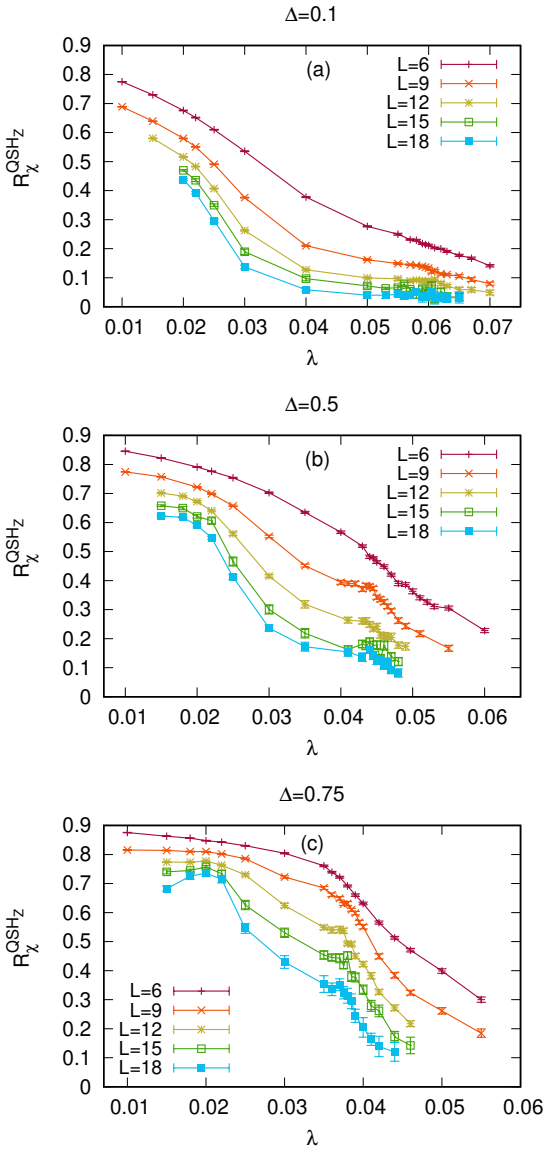


FIG. 19. Time displaced correlation ratio R_χ^{QSHz} for $\Delta = 0.1$ (a), $\Delta = 0.5$ (b), and $\Delta = 0.75$ (c), respectively.

Appendix C: Spectrum

The spectral function for a given operator at zero temperature reads:

$$A(\boldsymbol{k},\omega) = \pi \sum_n |\langle n|\hat{O}|0\rangle|^2 \delta(E_n - E_0 - \omega). \tag{C1}$$

Here, $|0\rangle$ in Eq. C1 denotes the ground state, and $|n\rangle$ denotes the eigenstates of the Hamiltonian with energy E_n. Given the imaginary-time Monte Carlo data, the spectrum is obtained using the stochastic analytical continuation approach[44] to solve for $A(\boldsymbol{k},\omega)$, given $\langle 0|\hat{O}^\dagger(\tau)\hat{O}(0)|0\rangle$:

$$\langle 0|\hat{O}^\dagger(\tau)\hat{O}(0)|0\rangle = \int d\omega e^{-\tau\omega} A(\boldsymbol{k},\omega). \tag{C2}$$

Here, $\hat{O}$ represents the momentum space operators defined in the main text: $\hat{J}^{XY}$, $\hat{\eta}$, $\hat{J}^Z$ and $\hat{c}$. $A(\boldsymbol{k},\omega)$ is the corresponding spectral function, denoted as A^{QSH}, A^{SSC}, A^{QSHz} and A^{sp}, respectively.

As expected, the single-particle spectrum A^{sp} is clearly gapped in both the QSH and SSC ordered states, as well as across the QSH-SSC transition points. As one can observe from Figs. 20, 21 and 22, A^{sp} shows no fundamental differences among three considered values of Δ.

Deep inside the ordered QSH and SSC phases, and irrespective of the anisotropy parameter, Δ, the order parameter excitations exhibit Goldstone modes stemming from global U(1) symmetry breaking. In particular, in Fig. 20, for the case $\Delta = 0.1$, a linear mode is observed for QSH operator at $\lambda = 0.04$ and for SSC operator at $\lambda = 0.065$. The same behavior is visible at $\Delta = 0.5$ and 0.75 in Fig. 21 and 22.

On the other hand, the excitation of both QSH and SSC order parameters at the critical point shows a linear dispersion relation. Near the Γ point, the Goldstone mode is expected to give rise to a branch cut reflecting the anomalous dimension:

$$\begin{aligned} A_{\mathrm{QSH}}(\boldsymbol{k},\omega) &\propto (v^2|\boldsymbol{k}|^2 - \omega^2)^{1-\frac{\eta_{\mathrm{QSH}}}{2}} \\ A_{\mathrm{SSC}}(\boldsymbol{k},\omega) &\propto (v^2|\boldsymbol{k}|^2 - \omega^2)^{1-\frac{\eta_{\mathrm{SSC}}}{2}}. \end{aligned} \tag{C3}$$

Although the anomalous dimension of the two order parameters can in general be different, the velocity v is uniquely defined at a Lorentz invariant critical point. We mark the velocity of these two excitations in Fig. 20, 21 and 22.

The spectrum of the Z component of the spin current operator ($\hat{J}^Z$) is controversial at the transition point. $A^{\mathrm{QSH}_Z}(\boldsymbol{k},\omega)$ shows a clear gap around the Γ point in the cases of $\Delta = 0.1$ and 0.5. On the other hand, we observe that the gap decreases upon reducing the anisotropy. As shown in Figs. 22 and 14 for $\Delta = 0.75$, the value of gap at the Γ point is comparable to the finite size gap of the superconducting fluctuations. A consistent picture in terms of easy-plane DQCP with deconfined spinons at criticality requires that the excitation gap of $\hat{J}^Z$ to scale to zero in the thermodynamic limit.

Appendix D: Local detection of Z_2 topology using π flux insertion

To detect the topology of our QSH insulator, we employ the magnetic flux insertion approach[45] that has successfully been tested in Ref. 31. When π fluxes are pumped locally into the QSH insulator, mid-gap states carrying nontrivial spin quantum numbers are exponentially localized around the flux insertion points. This approach directly probes the Z_2 topological invariant, and we refer the reader to Ref. 31 for a detailed discussion.

Consider the following kinetic Hamiltonian:

$$\hat{H}_t = -t \sum_{\langle \boldsymbol{i},\boldsymbol{j}\rangle} (\hat{\boldsymbol{c}}_{\boldsymbol{i}}^\dagger \hat{\boldsymbol{c}}_{\boldsymbol{j}} e^{iA_{ij}} + H.c.). \tag{D1}$$

and the interaction term:

$$\begin{aligned} \hat{H}_\lambda = -\lambda \sum_{\hexagon} \Bigg[&\left(\sum_{\langle\langle \boldsymbol{ij}\rangle\rangle \in \hexagon} \hat{J}^x_{\boldsymbol{i},\boldsymbol{j}} e^{iA_{ij}} \right)^2 + \left(\sum_{\langle\langle \boldsymbol{ij}\rangle\rangle \in \hexagon} \hat{J}^y_{\boldsymbol{i},\boldsymbol{j}} e^{iA_{ij}} \right)^2 \\ &+ \Delta \left(\sum_{\langle\langle \boldsymbol{ij}\rangle\rangle \in \hexagon} \hat{J}^z_{\boldsymbol{i},\boldsymbol{j}} e^{iA_{ij}} \right)^2 \Bigg] \end{aligned} \tag{D2}$$

where $\boldsymbol{A_{ij}}$ is the vector potential that accounts for the pair of π-fluxes. To practically insert a π-flux into our system, we consider an arbitrary string connecting the centers of the two hexagons. Each time an electron crosses this string, it acquires an $e^{i\pi}$ phase factor.

Due to the easy-plane anisotropy, the dynamical generation of the QSH insulator is associated with a long-range order of spin currents in the $U(1)$ plane. Thus, the mid-gap objects localized around the π fluxes are Kramers pairs of spin 'up' and 'down' states rotating in the $x-y$ plane, as well as doublets of charge fluxons. The presence of localized spin and charge fluxons can be captured by the low-energy spectral weight of $c_{\boldsymbol{i}}^\dagger \sigma^x c_{\boldsymbol{i}}$ ($c_{\boldsymbol{i}}^\dagger \sigma^y c_{\boldsymbol{i}}$) and $c_{\boldsymbol{i}}^\dagger c_{\boldsymbol{i}}$ operator:

$$\begin{aligned} S^{xy}_\Omega(\boldsymbol{i}) &\equiv \int_0^\Omega d\omega S^{xy}(\boldsymbol{i},\omega) \\ S^{\mathrm{charge}}_\Omega(\boldsymbol{i}) &\equiv \int_0^\Omega d\omega S^{\mathrm{charge}}(\boldsymbol{i},\omega) \qquad \Omega = 0.25 \end{aligned} \tag{D3}$$

where

$$\begin{aligned} S^{xy}(\boldsymbol{i},\omega) &= \pi \sum_n |\langle n|c_{\boldsymbol{i}}^\dagger \sigma^x c_{\boldsymbol{i}}|0\rangle|^2 \delta(\omega - E_n - E_0) \\ S^{\mathrm{charge}}(\boldsymbol{i},\omega) &= \pi \sum_n |\langle n|c_{\boldsymbol{i}}^\dagger c_{\boldsymbol{i}}|0\rangle|^2 \delta(\omega - E_n - E_0) \end{aligned} \tag{D4}$$

where $|n\rangle$ represents an energy eigenstate with energy E_n. The energy window of $\Omega = 0.25$ is well below twice single particle gap ($\Delta \approx 1.0$).

The enhanced spectral weight in $S^{xy}_\Omega(\boldsymbol{i})$ and $S^{\mathrm{charge}}_\Omega(\boldsymbol{i})$ around π fluxes, as depicted in Fig. 23, clearly demonstrates the existence of spin and charge fluxons. This

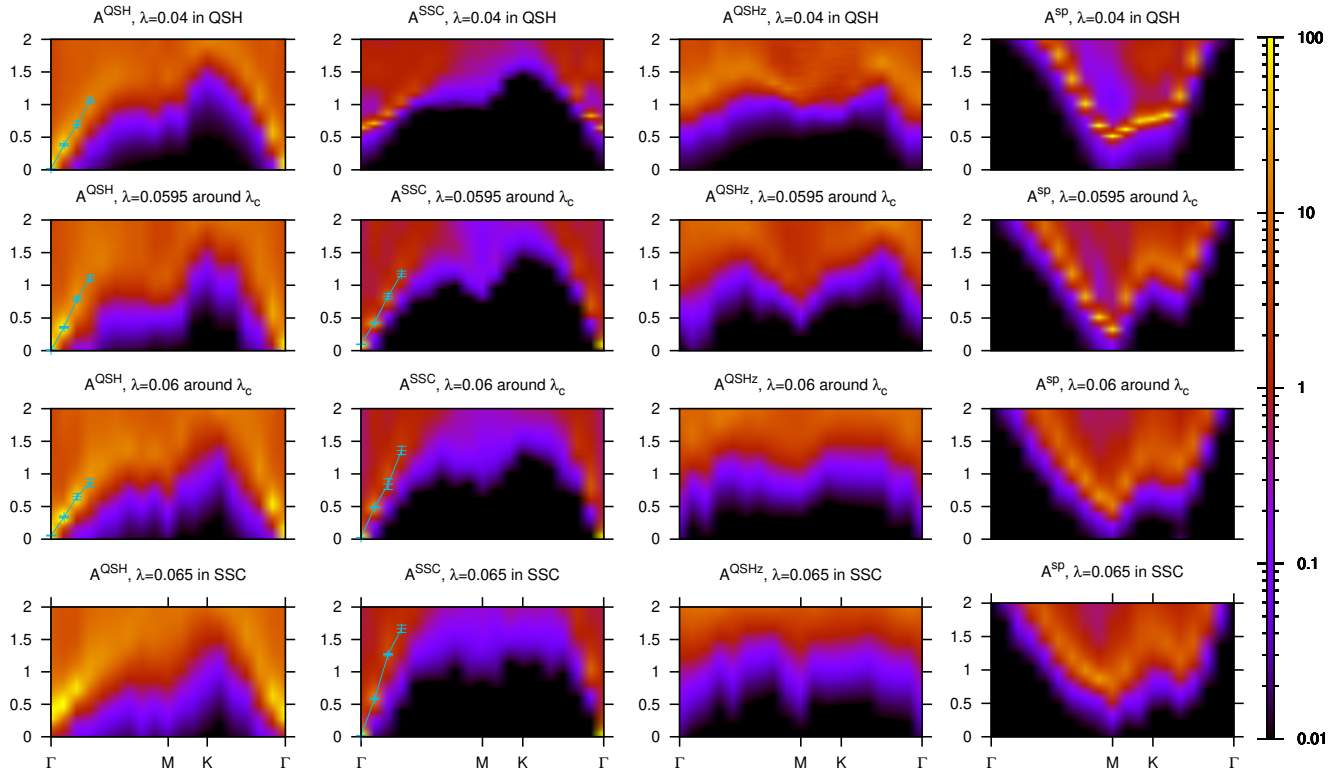


FIG. 20. QSH, SSC, QSHz, and single particle spectrum inside two (QSH, SSC) phases and near the critical point, for $\Delta = 0.1$. Blue lines are the momentum dependence of the extrapolated excitation gap of $\hat{J}$ and $\hat{\eta}^{+}(\hat{\eta}^{-})$ operators. We took $L = 18$.

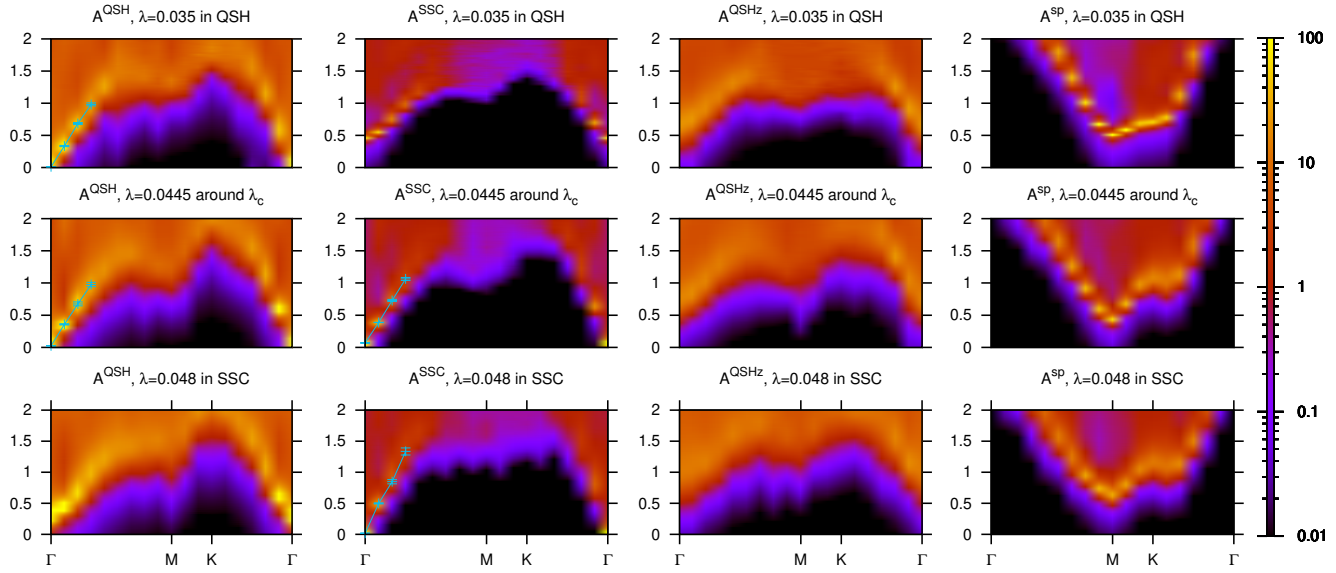


FIG. 21. Same as Fig. 20 for $\Delta = 0.5$.

numerically proves that the insulating state that we observe at intermediate values of λ is Z_2 nontrivial.

It is worth noting that our model does not exhibit quantized spin Hall conductivity due to the absence of $U(1)$ spin conservation at low energies. Therefore, the topological invariant characterizing our system is the Z_2 index, rather than the so-called spin Chern number.

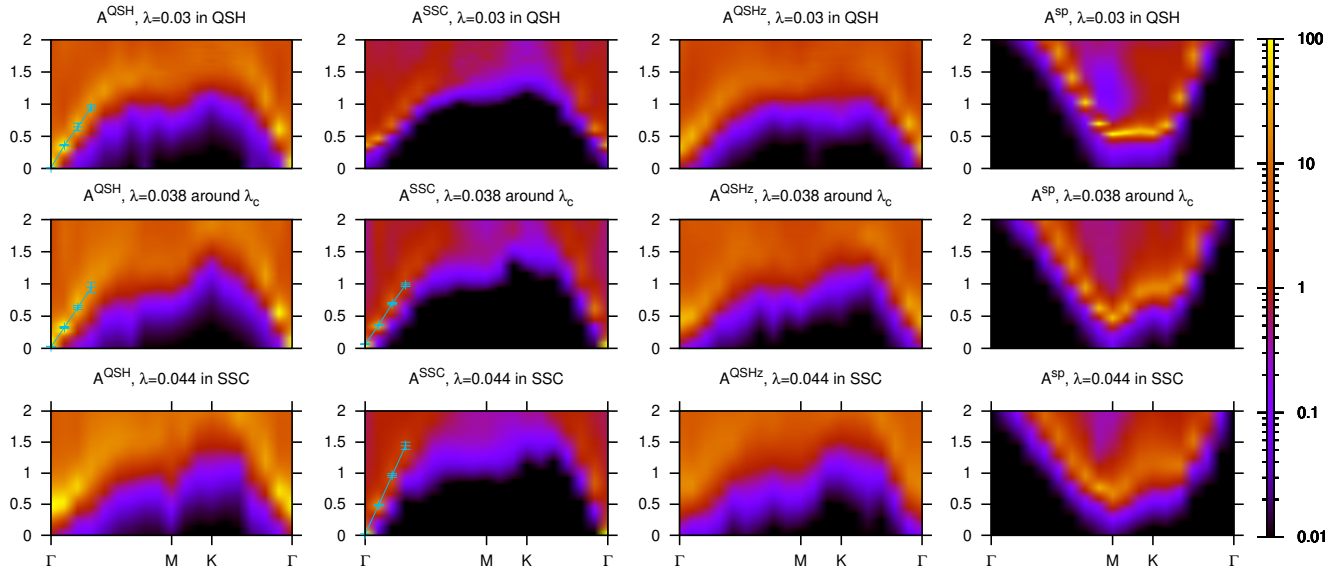


FIG. 22. Same as Fig. 20 for $\Delta = 0.75$.

Appendix E: Absence of monopoles

The aim of this section is to show the absence of monopoles in our system. A 'monopole' corresponds to a singularity of the $U(1)$ gauge field in CP^1 representation. It couples to the physical electric-magnetic vector potential such that a $U(1)$ electric-magnetic gauge invariance is broken in the presence of 'monopoles'.[5] Therefore, the statement of 'monopole-free' is a natural consequence of the exact $U(1)$ charge conservation in our physical system.

A continuum description of our system in terms of fluctuating QSH order parameter in S^2 space is:

$$S = \int d^2\boldsymbol{x} d\tau \psi^\dagger [\gamma_0\gamma_\mu(\partial_\mu + ieA_\mu) + im\boldsymbol{n}\cdot\gamma_0\gamma_3\gamma_5\vec{\sigma}]\psi + S_{\text{anisotropy}} + ... \tag{E1}$$

where $\psi(\boldsymbol{x},\tau)$ is the Grassmann variable in the space of $\mathbb{R}^2 \otimes \mathbb{C}^2_{valley} \otimes \mathbb{C}^2_{orbital} \otimes \mathbb{C}^2_{spin}$. $\boldsymbol{n}$ is the three-component order parameter of the QSH state and $S_{\text{anisotropy}}$ describes the anisotropic term which breaks SU(2) spin rotational symmetry down to U(1)×$\mathbb{Z}_2$. $A_\mu(\boldsymbol{x},\tau)$ is the physical electric-magnetic field. Note that our lattice model doesn't break particle number conservation, such that local $U(1)$ gauge symmetry is satisfied:

$$\begin{aligned}&\psi(\boldsymbol{x},\tau) \to e^{ie\theta(\boldsymbol{x},\tau)}\psi(\boldsymbol{x},\tau),\\ &A_\mu(\boldsymbol{x},\tau) \to A_\mu(\boldsymbol{x},\tau) - \partial_\mu\theta(\boldsymbol{x},\tau).\end{aligned} \tag{E2}$$

Since $\boldsymbol{n}$ is normalized to unity, the single particle gap does not close, and we can integrate out the fermions to obtain the effective action:

$$S = S_g + S_c \tag{E3}$$

where

$$S_g = \int d^2\boldsymbol{x} d\tau \frac{1}{m}[(\partial_\mu \boldsymbol{n})\cdot(\partial_\mu \boldsymbol{n})] \tag{E4}$$

and the lowest-order electric-magnetic response is

$$S_c = i\int d^2\boldsymbol{x}\int d\tau A^\mu(\boldsymbol{x},\tau)J^\mu(\boldsymbol{x},\tau) \tag{E5}$$

where

$$J^\mu(\boldsymbol{x},\tau) = 2e\frac{1}{8\pi}\epsilon^{\mu\alpha\delta}\boldsymbol{n}\cdot(\partial_\alpha\boldsymbol{n}\times\partial_\delta\boldsymbol{n}) \tag{E6}$$

Now reformulate the action into a gauge redundant (CP^1) representation:

$$\vec{N} \equiv z^\dagger\vec{\sigma}z \qquad z^\dagger z = 1 \tag{E7}$$

such that S_g is described by $\frac{1}{g}|(\partial_\mu - ia_\mu)z|^2$. A local $U(1)$ gauge redundancy comes naturally from the CP^1 reformulation:

$$z \longrightarrow e^{i\chi}z, \qquad a_\mu \longrightarrow a_\mu + \partial_\mu\chi \tag{E8}$$

Crucially the following identity holds:

$$\frac{1}{8\pi}\epsilon^{\mu\nu\lambda}\boldsymbol{n}\cdot(\partial_\nu\boldsymbol{n}\times\partial_\lambda\boldsymbol{n}) = \frac{1}{4\pi}\epsilon^{\mu\nu\lambda}\partial_\nu a_\lambda. \tag{E9}$$

This follows from the the saddle point results:[46]

$$a_\mu = iz^\dagger\partial_\mu z. \tag{E10}$$

To describe skyrmions one has to allow for compactness of a_μ :

$$\oint \boldsymbol{a}\cdot d\boldsymbol{l} = n2\pi \quad \text{with} \quad n\in\mathbb{Z} \tag{E11}$$

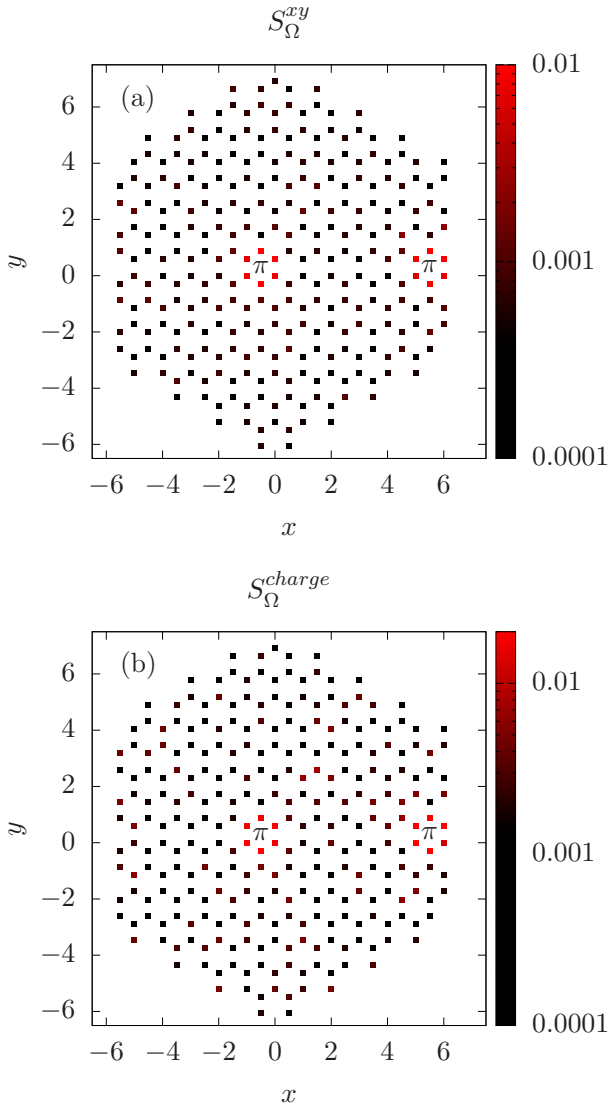


FIG. 23. $S^{xy}_{\Omega}(\boldsymbol{i})$ (a) and $S^{\text{charge}}_{\Omega}(\boldsymbol{i})$ (b) distributions on a $L = 12$ honeycomb lattice. The simulation is performed deep inside the QSH state ($\Delta = 0.1, \lambda = 0.045$). Here, $\beta = 24$.

for a closed loop. Using Stokes theorem, integration at a given time slice hence gives: $\int d^2\boldsymbol{x}\epsilon^{0\mu\nu}(\partial_\mu a_\nu - \partial_\nu a_\mu) = 4\pi n$ and counts the number of 'skyrmions' in the time slice. A magnetic 'monopole' corresponds to field configurations, a_μ, that have a non-vanishing 'magnetic flux', $\epsilon^{\delta\mu\nu}\partial_\mu a_\nu$, through a closed surface in space-time.

With Eq. E9 and Eq. E6, the Chern-Simons part of action reads

$$S_c = \int d^2\boldsymbol{x}d\tau \frac{ie}{2\pi}\epsilon^{\mu\nu\kappa}A_\mu\partial_\nu a_\kappa \tag{E12}$$

To show the absence of monopoles, we consider a uniform gauge transformation inside a sphere:

$$A_\mu \longrightarrow A_\mu + \partial_\mu\Theta \tag{E13}$$

with

$$\Theta(\tau, x, y) = \begin{cases} \Theta_0 & \text{for } r < R \\ 0 & \text{for } r \geq R \end{cases} . \tag{E14}$$

In the above $r = \sqrt{\tau^2 + x^2 + y^2}$. As a consequence, $\partial_\mu\Theta$ does not vanish only on sphere of radius R, S_R. In particular:

$$\begin{aligned} \delta S =& \frac{ie}{2\pi}\int d^3\boldsymbol{x}\epsilon^{\mu\nu\kappa}\partial_\mu\Theta\,\partial_\nu\, a_\kappa \\ =& \frac{ie}{2\pi}\Theta_0\int_{S_R} d\boldsymbol{s}_\mu\epsilon^{\mu\nu\kappa}\partial_\nu\, a_\kappa \\ \equiv& \frac{ie}{2\pi}\Theta_0 Q. \end{aligned} \tag{E15}$$

In the above, $d\boldsymbol{s}$ defines a surface element of S_R and Q the number of monopoles within S_R. If $Q \neq 0$ then U(1) local gauge invariance (see Eq. E2) is not satisfied. Hence, charge conservation, or equivalently U(1) local gauge invariance, requires $Q = 0$ and the absence of monopoles.

It is important to emphasize that, based on spin coherent path integral calculation by Haldane,[47] the monopole configurations of anti-ferromagnetically coupled spin 1/2 system on the square lattice also carry a nontrivial phase factor upon a $U(1)$ gauge transformation. However, in this case, instead of the physical electromagnetic field, this $U(1)$ transformation corresponds to the lattice rotation. This symmetry is broken upon lattice regularization, and only a Z_4 subgroup of it is conserved. Under $\pi/2$ lattice rotation, a single monopole contributes by

$$\delta S = i\frac{\pi}{2} \tag{E16}$$

to the action. Hence, quadruple monopoles configurations are allowed.